Icarus 223 (2013) 234–251

Contents lists available at SciVerse ScienceDirect

Icarus

journal homepage: www.elsevier.com/locate/icarus

On the thermal electron balance in Titan's sunlit upper atmosphere

E. Vigren [a,*], M. Galand [a], R.V. Yelle [b], J. Cui [c,d], J.-E. Wahlund [e], K. Ågren [e], P.P. Lavvas [f], I.C.F. Mueller-Wodarg [a], D.F. Strobel [g], V. Vuitton [h], A. Bazin [h]

[a] Department of Physics, Imperial College, London SW7 2AZ, UK
[b] Lunar and Planetary Laboratory, University of Arizona, Tucson, AZ 85721-0092, USA
[c] School of Astronomy and Space Sciences, Nanjing University, Nanjing 210008, China
[d] National Astronomical Observatories, Chinese Academy of Sciences, Beijing 100012, China
[e] Swedish Institute of Space Physics, Uppsala, Sweden
[f] Groupe de Spectrométrie Moléculaire et Atmosphérique, Université Reims Champagne-Ardenne, UMR 7331, Reims 51687, France
[g] Department of Earth & Planetary Sciences, Johns Hopkins University, Baltimore, MD 21218, USA
[h] Institut de Planétologie et d'Astrophysique de Grenoble (IPAG), UJF-Grenoble/CNRS-INSU, UMR 5274, Grenoble F-38041, France

ARTICLE INFO

Article history:
Received 15 August 2012
Revised 5 November 2012
Accepted 12 December 2012
Available online 23 December 2012

Keywords:
Titan
Ionospheres
Atmospheres, Chemistry

ABSTRACT

The Cassini mission has investigated Titan's upper atmosphere in detail and found that, under solar irradiation, it has a well-developed ionosphere, which peaks between 1000 and 1200 km. In this paper we focus on the T40, T41, T42 and T48 Titan flybys by the Cassini spacecraft and use *in situ* measurements of N_2 and CH_4 densities by the Ion Neutral Mass Spectrometer (INMS) as input into a solar energy deposition model to determine electron production rates. We combine these electron production rates with estimates of the effective recombination coefficient based on available laboratory data for Titan ions' dissociative recombination rates and electron temperatures derived from the Langmuir probe (LP) to predict electron number densities in Titan's upper atmosphere, assuming photochemical equilibrium and loss of electrons exclusively through dissociative recombination with molecular ions. We then compare these predicted electron number densities with those observed in Titan's upper atmosphere by the LP. The assumption of photochemical equilibrium is supported by a reasonable agreement between the altitudes where the electron densities are observed to peak and where the electron production rates are calculated to peak (roughly corresponding to the unit optical depth for HeII photons at 30.38 nm). We find, however, that the predicted electron number densities are nearly a factor of two higher than those observed throughout the altitude range between 1050 and 1200 km (where we have made estimates of the effective recombination coefficient). There are different possible reasons for this discrepancy; one possibility is that there may be important loss processes of free electrons other than dissociative recombination in Titan's upper atmosphere.

1. Introduction

Titan is the largest satellite of Saturn and the only satellite in the Solar System to hold a dense and permanent atmosphere. The Cassini mission has considerably improved and challenged our understanding of Titan's upper atmosphere. Solar EUV photons and soft X-rays and energetic charged particles from Saturn's magnetosphere ionize, excite, and dissociate N_2 and CH_4, the main constituents of Titan's upper atmosphere. This initiates a network of chemical reactions, forming the most chemically complex ionosphere in the Solar System, including long-chain hydrocarbons, aromatic molecules and nitrogen containing (in particular nitrile-) molecules (e.g., Vuitton et al., 2007). Ion chemistry acting in Titan's upper atmosphere is a significant source of Titan's aerosols, which ultimately precipitate to the surface of the Moon (Waite et al., 2007; Vuitton et al., 2008; Wahlund et al., 2009). In this paper we challenge our understanding of Titan's dayside ionosphere. More specifically the goal is to test the ability to accurately predict electron number densities in the dayside ionosphere of Titan following assumptions of photochemical equilibrium and loss of free, thermal electrons exclusively by dissociative recombination with molecular ions. We focus in particular on four Titan flybys by the Cassini spacecraft (T40, T41, T42 and T48) and for each flyby we use a multi-instrumental Cassini dataset, accurate information on the impinging solar EUV/XUV spectra as observed from Earth and extrapolated to Saturn, laboratory data of photo- and electron-impact processes and of dissociative recombination reactions, and a solar energy deposition model (based on Galand et al.,

* Corresponding author.
E-mail address: e.vigren@imperial.ac.uk (E. Vigren).

0019-1035/$ - see front matter © 2012 Elsevier Inc. All rights reserved.
http://dx.doi.org/10.1016/j.icarus.2012.12.010

2010) that combined gives the opportunity to predict electron number densities within a well-constrained parameter space.

Solar photons are the main source of ionization on the dayside, and even somewhat beyond the terminator due to the extended nature of Titan's atmosphere (see e.g., Ågren et al., 2009; Galand et al., 2006, 2010; Robertson et al., 2009; Kliore et al., 2011; Luhmann et al., 2012). This and the fact that Titan's ionosphere is dominated by molecular ions that have large electron recombination rate coefficients (Cravens et al., 2005; Vuitton et al., 2006, 2007) yielding short chemical lifetimes, implies that the ionosphere should be Chapman-like, by which we mean that the electron density profile is determined by a local balance between solar photo-ionization and recombination. This behavior is indeed supported by the variations of the magnitude and the altitude of the peak electron density with solar zenith angle in Titan's ionosphere (Ågren et al., 2009).

The continuity equation applied to the electron number density, n_e, is given by

$$\frac{\partial n_e}{\partial t} + \nabla \cdot (n_e \mathbf{u_e}) = P_e - n_e L_e \quad (1)$$

where P_e ($cm^{-3}\ s^{-1}$) and L_e (s^{-1}) are the electron production and loss rates, respectively, and the second term on the left-hand side is the flux divergence with $\mathbf{u_e}$ being the electron drift velocity. When charge balance applies and electrons are lost exclusively through recombination with molecular ions, L_e in Eq. (1) can be expressed as $n_e\alpha_{eff}$ where α_{eff} is the effective recombination coefficient (for definition see Eq. (4)). The peak electron density in Titan's dayside ionosphere is roughly 2500 cm^{-3}. Adopting 5×10^{-7} $cm^3\ s^{-1}$ as a typical recombination rate coefficient implies a recombination time constant of about 800 s, which is about three orders of magnitude shorter than a Titan day and consequently diurnal variations should not affect the dayside electron densities significantly, i.e. the time dependent term of Eq. (1) may be neglected. Another requirement for a local balance between photo-ionization and recombination is that chemistry dominates over transport, i.e. that the flux divergence term in Eq. (1) may be neglected. Ma et al. (2006) investigated this question and found that chemistry should dominate over transport below about 1300 km (see also Robertson et al., 2009; Cravens et al., 2010). As we primarily focus our studies to altitudes below 1200 km Eq. (1) then takes the simple form of local balance between electron production and loss rates:

$$P_e(z) = n_e(z) L_e(z) \quad (2)$$

Ågren et al. (2009) showed that nightside n_e values are about 20% of the dayside values. The nightside ions are likely due to a combination of ionization from magnetospheric auoral electrons (and their secondaries) (e.g., Cravens et al., 2005, 2009) and survival of some long-lived dayside ions through the Titan night (Cui et al., 2009, 2010). The contribution of magnetospheric electrons to the dayside electron production rate is, however, expected to be small (about 5%) as further discussed in Section 3.3. These arguments apply to the mean ionosphere between about 1050 and 1200 km. Negative ions have been observed to exist in high abundances near 1000 km and below (Coates et al., 2007; Ågren et al., 2012) while transport becomes important at higher altitudes.

Following these lines we anticipate Titan's ionosphere to be Chapman-like, in accordance with other ionospheres in the Solar System, such as the E region of the terrestrial ionosphere, and regions of the ionospheres of Mars and Venus (e.g. Rasmussen et al., 1988; Mendillo et al., 2011; Fox, 2007). Local balance between solar-driven ionization and recombination implies, as mentioned, specific relationships for the variation of the peak value of n_e and the altitude of the n_e peak with solar zenith angle. This behavior has been demonstrated in several studies of the martian ionosphere (see e.g., Fox and Yeager, 2006; Martinis et al., 2003; Mendillo et al., 2011) and for Venus at least in terms of how the peak values of n_e vary with SZA. A non-Chapman behavior has been observed in terms of how the peak altitudes of n_e vary with SZA in the venusian ionosphere, being at a nearly constant level of 140 km as the SZA increases from about 25° to 70° and then decreasing slightly to 135 km as the SZA increases from 70° to 85° (Cravens et al., 1981). This behavior may be ascribed to the variations of the near-terminator thermosphere, in which the values of the neutral densities decrease with increasing SZA (Fox, 2007; Cravens et al., 1981). It is noted that photochemical equilibrium models of the dayside martian and venusian lower ionospheres have been found to reproduce measured electron densities typically better than to within 25% and clearly within the error bars of the model predictions and observations (for Mars e.g., Mendillo et al., 2011; Fox and Yeager, 2006, for Venus e.g., Cravens et al., 1981; Fox, 2007). This high accuracy is possible because the dominance of local chemistry lessens or removes uncertainties due to diffusion rates, advection velocities, and magnetic topology. Counterexamples are seen in the ionospheres of the giant planets where H^+, a major ion, has a long lifetime. These ionospheres are severely more complicated to model due to the presence of strong winds and also due to the limited knowledge of the abundance of vibrationally excited H_2 molecules ($v \geqslant 4$) and the inflow of water molecules, both of which effectively can convert H^+ to shorter-lived molecular ions and thereby strongly affect the predicted electron number densities (see e.g., Yelle and Miller, 2004; Moore et al., 2010 and references therein, Moses and Bass, 2000; Waite et al., 1997 and references therein).

To simplify Chapman-like ionospheres even further an effective recombination coefficient may be adopted to avoid dealing with numerous ion-neutral reactions. This leads to the following expression for the electron number density (e.g., Galand et al., 2010):

$$n_e(z) = \sqrt{P_e(z)/\alpha_{eff}(z)} \quad (3)$$

where P_e is the electron production rate and where the effective recombination coefficient, α_{eff}, here is defined as the weighted average

$$\alpha_{eff}(z) = \frac{\sum_j \alpha_j(T_e) n_j(z)}{\sum_j n_j(z)} \quad (4)$$

where the sums are over all positive ions j, n_j is the number density and $\alpha_j(z)$ is the dissociative recombination rate coefficient of ion species j, which primarily depends on the ambient electron temperature, T_e.

The concept of an effective recombination coefficient is not really needed on Mars and Venus where O_2^+ strongly dominates the ionospheric composition in the regions where photochemical equilibrium may be assumed, but it has proven useful for the terrestrial ionosphere. In the E-region of Earth's ionosphere the dominant ions are NO^+ and O_2^+. As the rate coefficient for dissociative recombination of NO^+ is about twice that of O_2^+, knowing the relative abundances of NO^+ and O_2^+, which vary with solar activity and season (e.g., Titheridge, 1997), is necessary for estimating electron number densities accurately. In addition below 80 km in the D-region of Earth's ionosphere, the increased relative abundances of hydrated cluster ions, with significantly higher dissociative recombination rate coefficients than O_2^+ and NO^+, must be taken into consideration to enable more accurate n_e predictions (e.g., Osepian et al., 2009). For Titan's ionosphere an effective recombination coefficient is indeed a very useful approximation because it eliminates the need to accurately model the complex chemistry if only the electron density is of interest. For example, an effective recombination rate approximation has been used in models of Titan's magnetospheric interaction where the added computation burden

of modeling the chemistry is difficult to include and of secondary interest (e.g., Ma et al., 2006).

To assess the effective recombination coefficient in Titan's ionosphere we benefit from (1) previously published (e.g., Cui et al., 2009) ion density measurements by the Ion Neutral Mass Spectrometer (INMS) in its open source (OSI) mode, (2) from the chemical assigning of ions with different mass-to-charge ratios (Vuitton et al., 2006, 2007) and (3) from laboratory derived rate coefficients for the dissociative recombination of the dominant ions in Titan's upper atmosphere. This allows first of all to estimate $\alpha_{eff,300}(z)$, the effective recombination coefficient at a reference electron temperature of 300 K as a function of altitude (see Section 4). We select a reference electron temperature of 300 K for convenience as most experimentally derived rate coefficients are presented on the form $\alpha_{300} \times (T_e/300)^{\beta}$ with α_{300} being the rate coefficient at $T_e = 300$ K and with $(T_e/300)^{\beta}$ describing the electron temperature dependence of the reaction. As justified in Section 5.4.2.1, we adopt an electron temperature dependence of the effective recombination coefficient of $(T_e/300)^{-0.7}$. From this Eq. (3) can be rewritten as

$$n_{e,Model}(z) = \sqrt{\frac{P_e(z)}{\alpha_{eff,300}(z) \times (T_e(z)/300)^{\beta}}} \quad (5)$$

where $P_e(z)$ is the solar-driven electron production rate at altitude z, $\alpha_{eff,300}(z)$ is the effective electron recombination coefficient at z at a reference electron temperature of 300 K, $T_e(z)$ is the electron temperature derived from the Langmuir probe at z and $\beta = -0.7$, is a typical value describing the power law dependence of the dissociative recombination rate coefficient for the dominant ions in Titan's ionosphere.

There have been a number of previous attempts to model the electron number density in Titan's upper atmosphere based on Cassini data. For the first close Titan flyby, TA (reaching 1174 km at closest approach), Cravens et al. (2005) calculated the electron number density using an electron transport model combined with a photochemical ionospheric model driven by INMS derived N_2 and CH_4 densities. The resulting electron number densities were compared with the electron densities observed by the Langmuir probe (LP) (Wahlund et al., 2005). On the sunlit path of the flyby (inbound) with 80° < SZA < 90°, the model underestimated the observations by approximately 30% when solar radiation was the only energy source considered. Robertson et al. (2009) applied a similar approach to the T17 and T18 Titan flybys and showed that at altitudes below about 1100 km the modeled electron densities were significantly higher than those observed by the LP. Galand et al. (2010) focused on the T18, T32, T39 and T40 Titan flybys. They derived effective recombination coefficients based on observed electron densities and calculated electron production rates. They found that the effective recombination coefficients agreed well with predicted values based on the ion composition at 1200 km. The agreement with such predictions got, however, progressively worse towards lower altitudes implying an overestimation of modeled n_e compared with those observed.

Since the publication of these works, however, the INMS instrument has been re-calibrated implying that the previously used N_2 and CH_4 densities were too low by a factor of about 2.9 (see Section 2.2.1). With the updated neutral density profiles, the resulting P_e(z) calculations, combined with our estimates of $\alpha_{eff,300}(z)$ and the LP-derived T_e values, results (using Eq. (5)) in predicted n_e profiles which in a relative sense match those observed by the LP fairly well, therefore pointing towards a Chapman-like behavior of the ionosphere. This is illustrated in Fig. 1 across the altitude range from closest approach to 1400 km for the inbound parts of T40, T41 and T42 and the outbound leg of T48, though it is emphasized that it is pre-dominantly below about 1300 km such a Chapman-like behavior is anticipated where photochemical equilibrium conditions are expected to prevail. The parameters used to produce the graphs in Fig. 1 are described in Section 5.2.

The most striking aspect of Fig. 1 is the fact that our model clearly over-predicts the observed electron number densities. The disagreement is large, roughly a factor of 2. This can be contrasted with the good agreement between models and observations of the n_e profiles in the ionospheres of Venus and Mars. Stated in another way, the effective recombination coefficient in Titan's ionosphere inferred from measured electron number densities and computed ionization rates are about a factor of 4 times higher than anticipated from laboratory measurements, certainly much larger than the uncertainties of these recombination rate coefficients.

This paper presents an investigation into this surprising problem with the electron densities in Titan's ionosphere by studying the uncertainties in the local balance model. We evaluate primarily uncertainties in neutral atmospheric densities, the impinging solar EUV/XUV spectra (both of which affect the electron production rates), the electron densities and temperatures, and the recombination rates. We show that systematic errors of these parameters are unlikely to explain the large discrepancy found between observed and modeled n_e values, so we argue that something additional must be considered as well, such as an unidentified chemical process increasing the loss rate of thermal electrons.

The outline of the paper is as follows: In Section 2 we describe the individual Titan flybys (T40, T41, T42 and T48) that are mainly used in the study and present the Cassini dataset relevant for the calculations of electron production rates (and our predictions of the electron number densities). In addition we present the electron densities as derived from the LP onboard Cassini, with which we later compare our predicted electron number densities. In Section 3 (and in Appendix A) we present the solar energy deposition model used to calculate electron production rates. In Section 4 we derive estimates of $\alpha_{eff,300}(z)$. In Section 5 we present the calculated electron production rates and the derived electron number densities and make in particular two types of comparisons. In Section 5.1 we compare the altitudes where the electron densities are observed to peak with the altitudes where we calculate the electron production rates to peak. In Section 5.2 we compare the $n_{e,LP}$ values (the observed n_e values as derived from the LP) with the predicted $n_{e,Model}$ values as given by Eq. (5) and highlight that the latter overpredicts the former. In Section 5.3 we show that the issue of overpredicted n_e values also appears for other dayside Titan flybys (T36, T39 and T43) that occurred at somewhat different geometrical conditions than the set of four flybys we are mainly focusing on. In Section 5.4 we discuss possible reasons for the discrepancy found between the magnitude of $n_{e,Model}(z)$ and the observed electron number densities. Conclusions are given in Section 6.

2. Flyby characteristics and Cassini dataset

2.1. Flyby characteristics

We study Titan flybys by the Cassini spacecraft during which both the INMS and the LP operated and where the relevant data, i.e. N_2 and CH_4 number densities, electron number densities and temperatures, have been extracted. In addition we focus only on flybys reaching deep into the ionosphere, as we are interested in the region where we anticipate photochemical equilibrium to apply. Finally we select flybys with low solar zenith angles (below 50°) to ensure that non-solar-ionization sources only plays a minor role in the electron production. The resulting seven Titan flybys (or flyby parts) are T36 (outbound), T39 (outbound), T40, T41, T42, T43 and T48. Among these there are four flybys, namely T40, T41, T42 and T48, which occurred at quite similar conditions, all in 2008 (during solar minimum conditions), between 10 and 11.30 Saturn

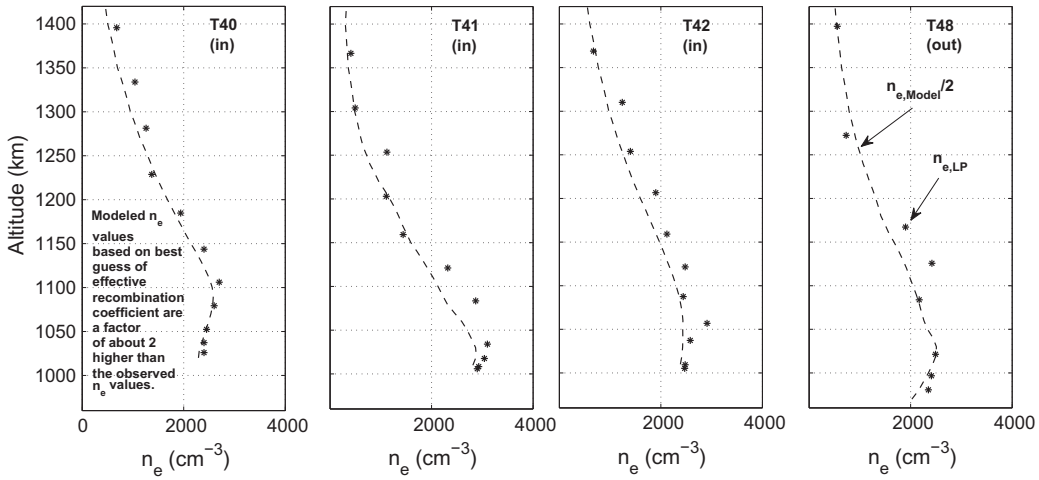

Fig. 1. LP-derived electron number densities (asterisks) and model derived values divided by 2 (dashed lines) versus altitude for the T40 (inbound), T42 (inbound) and T48 (outbound) Titan flybys by the Cassini spacecraft. The modeled values are based on Eq. (5) with P_e calculated as described in Section 3, T_e being taken from the fits of the LP-derived T_e-data shown in Fig. 4 for these particular flyby parts, and with $\alpha_{eff,300}$ treated as constant above 1200 km and below 1050 km, and according to Eq. (10) in between 1050 and 1200 km.

local time, from low to mid latitudes in the southern hemisphere and between the wake and the anti-Saturn region. In the present study we focus primarily on these four flybys, the relevant data of which are presented in Table 1 and Fig. 2. In Section 5.3 we present in a more concise manner results associated with the T36 (outbound), T39 (outbound) and T43 Titan flybys.

2.2. Cassini dataset

2.2.1. Ion Neutral Mass Spectrometer (INMS)

The INMS, which can be run in a closed source neutral (CSN) mode and an open source ion (OSI) mode, is described in detail in e.g., Waite et al. (2004). For the present study we are mainly interested in the density profiles of the dominant atmospheric species, N_2 and CH_4. We use in this study updated density profiles for these species, the retrieval of which is described in Cui et al. (2012). Compared with earlier derived neutral densities (as used for instance in Galand et al. (2010)) these densities are higher by about a factor of 2.9 following a recent re-calibration of the INMS instrument (see also Westlake et al., 2012; Richard et al., 2011; Koskinen et al., 2011). The density profiles for N_2 and CH_4 derived for the T40, T41, T42 and T48 flybys are shown in Fig. 2. Fig. 2 also shows the column density of N_2 in the line of sight towards the Sun as inferred from the N_2 density measurements, taking into account the solar zenith angle at each point along the Cassini trajectory.

As statistical uncertainties are small for the INMS measurements the overall uncertainty to the density values we are using is likely dominated by the potential error in the choice of the introduced density correction factor: 2.9. This value matches the one derived by Koskinen et al. (2011) who compared the INMS total densities and the Cassini Ultraviolet Spectrograph (UVIS) values for the T41 flyby. Moreover, matching INMS total densities to the values inferred from the Cassini Attitude and Articulation Control Subsystem (AACS) and the Huygens Atmosphere Structure Instrument (HASI) suggests a correction factor of about 2.6 (Strobel, 2010), i.e. only 10% lower than the correction factor used to derive the density profiles employed in this work. We deem it unlikely that the densities we are using are off by more than 20%, a statement which is further strengthen in Section 5.1.

Table 1
Titan flybys and their dates with information on the Saturn local time (SLT) and the solar zenith angle (SZA), latitude, longitude and altitude at closest approach (C/A).

Flyby	SLT (h)	SZA (°)	Lat. (°)	Long. (°)	Alt. (km)
T40 (January 5, 2008)	11.33	38	12(S)	130	1014
T41 (February 22, 2008)	11.22	30	35(S)	152	1000
T42 (March 25, 2008)	11.12	21	27(S)	157	999
T48 (December 5, 2008)	10.37	25	10(S)	178	961

2.2.2. Langmuir probe (LP)

The 5 cm diameter spherical Langmuir probe (LP) sensor (a subsystem of the Cassini Radio and Plasma Wave Science (RPWS) experiment) is mounted on a boom and situated 1.5 m from the main body of the Cassini spacecraft. It is used for *in situ* measurements of electron density (n_e) and temperature (T_e). Wahlund et al. (2009) and Ågren et al. (2009) describe how n_e and T_e are derived from voltage sweeps (typically ±4 V) every 24 s during Titan flybys. Between these voltage sweeps the LP also samples continuous density data at a frequency of 20 samples/s and at a fixed bias voltage (typically +4 V). The n_e and T_e values derived from the voltage sweeps are primarily used in this study, but the data collected in the continuous mode has been used in addition to the sweep data to set constraints on the altitude of maximum electron density observed during the studied Titan flybys (see Section 5.1 and Ågren et al., 2009). Figs. 3 and 4 show the LP derived electron densities (sweep mode) and electron temperatures associated with the T40, T41, T42 and T48 Titan flybys near 1400 km and below. Note that we primarily make use of the values below 1200 km. Uncertainties of <10% and <20% are expected for the n_e and T_e values, respectively (Ågren et al., 2009).

3. Calculation of electron production rates

We consider only solar ionization sources and calculate the electron production rate $P_e(z)$ as the sum of the primary (or photo-) electron production rate, $P_{e,\mathrm{prim}}(z)$, and the secondary electron production rate (due to electron impact ionization caused by photoelectrons and their secondaries), $P_{e,\mathrm{sec}}(z)$. The calculations of $P_{e,\mathrm{prim}}(z)$ are explained in Section 3.1 (see also Galand et al., 2010) and the calculations of $P_{e,\mathrm{sec}}(z)$ are explained in Section 3.2 and in Appendix A.

3.1. Photoelectron production rate ($P_{e,prim}$)

Observations from the Thermosphere Ionosphere Mesosphere Energetics and Dynamics (TIMED)/Solar EUV Experiment (SEE)

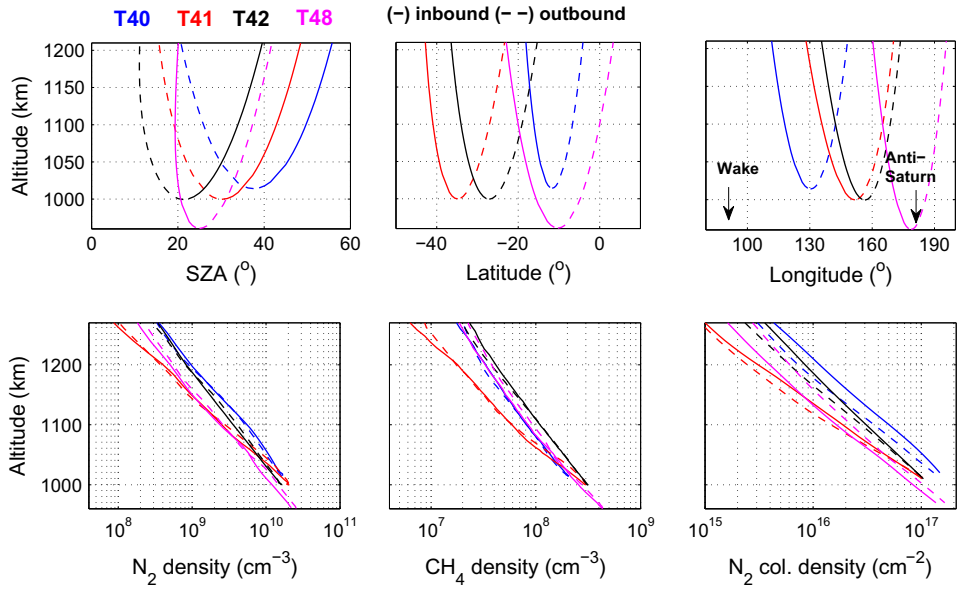

Fig. 2. Flyby geometry and neutral density data for the T40 (blue), T41 (red), T42 (black) and T48 (magenta) Titan flybys. Solid and dashed lines refer to the inbound and outbound parts of the flybys, respectively. Shown in the different panels against altitude along the Cassini trajectory are solar zenith angle (SZA), latitude, longitude, N_2 number density, CH_4 number density and column density of N_2 in the line of sight towards the Sun. (For interpretation of the references to color in this figure legend, the reader is referred to the web version of this article.)

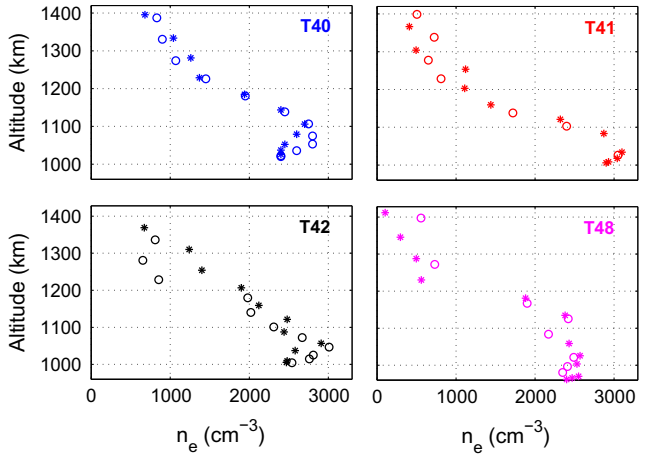

Fig. 3. Electron number density versus altitude along the Cassini trajectory derived from LP measurements for the T40, T41, T42 and T48 Titan flybys. Asterisks (*) and open circles (o) are for inbound and outbound points, respectively.

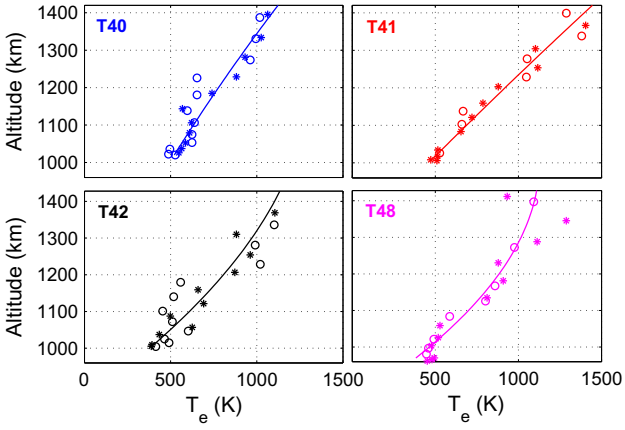

Fig. 4. Electron temperature versus altitude along the Cassini trajectory derived from LP measurements for the T40, T41, T42 and T48 Titan flybys. Asterisks (*) and open circles (o) are for inbound and outbound points, respectively. The solid blue line is the best fit to a second order polynomial function of the inbound T_e values for the T40 flyby. The red, black and magenta-colored lines are the corresponding best fits of the T_e data for the inbound legs of T41 and T42 and the outbound leg of T48, respectively. These best-fit-functions were used in the generation of the $n_{e,Model}$ graphs shown in Fig. 1. (For interpretation of the references to color in this figure legend, the reader is referred to the web version of this article.)

(Level 3) extrapolated in distance and phase to Saturn provides the solar irradiance (expected to be accurate to within about 20%) in 1 nm intervals impinging upon Titan's ionosphere of relevance for our studies (Woods et al., 2005; Woods, 2008; Lean et al., 2011). Noteworthy N_2 and CH_4 can only be ionized by photons of wavelengths lower than approximately 79.6 and 98.0 nm, respectively. An instrumental error affects the TIMED/SEE measurement in the 60.0–61.0 and 61.0–62.0 nm intervals (increased noise due to detector degradation) and below 27.0 nm (in the XUV range) the dataset is partly based on model calculations (see Galand et al., 2009; Woods et al., 2008). Fig. 5 provides information on the XUV/EUV solar fluxes for the days corresponding to the T40, T41, T42 and T48 flybys. The high flux value in the 30.0–31.0 nm wavelength bin is due to the strong solar HeII line at 30.38 nm and the high flux in the 97.0–98.0 nm wavelength bin is mainly attributed to the CIII line at 97.70 nm. Although photons from the solar CIII line can ionize CH_4, the ionization yield at this wavelength is small. Significant ion production commences only below about 65 nm and 80 nm for N_2 and CH_4, respectively (e.g., Rees, 1989; Lavvas et al., 2011). With regard to the solar variability the integrated flux below 80 nm was highest for the day corresponding to T40 and lowest for the day corresponding to T48. Defining F_X as the integrated flux below X nm it is noted that F_{80}(T40)/F_{80}(T41), F_{80}(T40)/F_{80}(T42) and F_{80}(T40)/F_{80}(T48) were 1.08, 1.03 and 1.26, respectively.

The photoelectron energy spectrum and the photoelectron production rate, $P_{e,\mathrm{prim}}(z)$, at altitude z is determined from the Beer–Lambert law (e.g., Rees, 1989). For these calculations we incorporate information on the solar zenith angle and the TIMED/SEE derived XUV/EUV fluxes at the top of the atmosphere (we have

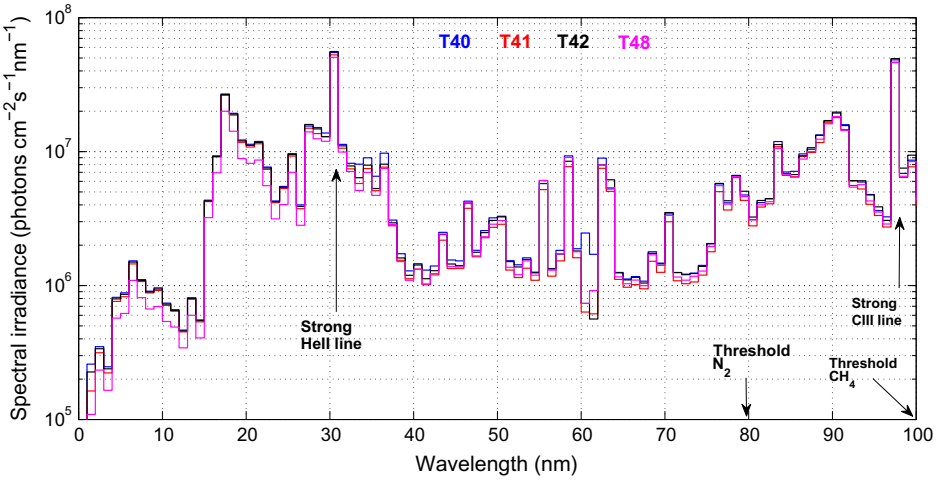

Fig. 5. Spectral irradiance derived from TIMED/SEE and used in the calculation of the electron production rates for the T40 (blue), T41 (red), T42 (black) and T48 (magenta) flybys. Indicated in the figure are also the lowest threshold energies for photoionization of N_2 and CH_4. (For interpretation of the references to color in this figure legend, the reader is referred to the web version of this article.)

used z_{top} = 1500 km, but it is noted that using z_{top} = 1400 km gives very similar values of $P_{e,\mathrm{prim}}(z)$ at altitudes below 1200 km). We also use the INMS derived densities of N_2 and CH_4 (treated as constant in spherical shells) and a set of photoabsorption/photoionization processes for N_2 and CH_4, their energy dependent absolute cross sections and their threshold energies. As for the latter we have used the same cross sections and threshold energies as Galand et al. (2010), which are based on Samson et al. (1987, 1989) and Stolte et al. (1998). Lavvas et al. (2011) showed that using a theoretically derived high-resolution N_2 neutral photodissociation cross section set (above 80 nm), affected the predicted photolysis rates of both N_2 and CH_4 in Titan's upper atmosphere. The total electron production rates, however, are not significantly affected by the consideration of this high-resolution cross section set.

3.2. Secondary electron production rate ($P_{e,sec}$)

The secondary electron production rate, $P_{e,\mathrm{sec}}$, due to electron impact ionization occurring during the electron energy degradation of photoelectrons and their secondaries have been calculated in a simplified manner. We have used the local approximation, i.e., we assume that electrons produced locally also are lost locally. This is a valid approximation at least below 1200 km (e.g., Lavvas et al., 2011) where neutral densities are sufficiently high to give electrons mean free paths of less than 20 km. We refer the reader to Appendix A for a description of the electron energy degradation (EED) model and its further simplifications and approximations. Here we only discuss the electron-impact processes and the cross section set used in the calculations (Section 3.2.1), and how the secondary electron production rates calculated with the EED model compares with those from a more detailed approach (Section 3.2.2).

3.2.1. Electron impact processes

We have taken the electron impact processes, their cross sections and excitation/ionization energies from Lavvas et al. (2011), who in turn used Itikawa (2006) and Shemansky and Liu (2005) as references for N_2 cross sections and Liu and Shemansky (2006) and Erwin and Kunc (2005, 2008) as references for CH_4 cross sections. We have also added excitation into a few additional $^1\Pi_u$ states of N_2 based on Majeed and Strickland (1997). Furthermore, we neglected pure rotational excitations, as the electron energy loss is small in these processes ($\approx 10^{-3}$ eV). We have neglected pure vibrational excitations for two reasons. First of all the electron energy losses associated with these processes are relatively low ($\approx 10^{-1}$ eV). It is also noted that for electron energies above 12.7 eV the peak cross section for the vibrational excitation ($v = 0 \rightarrow 1$) of N_2 is $\approx 2 \times 10^{-17}$ cm^2 and occurs at about 20 eV. This is already lower than the total ionization cross section at that energy ($\approx 2.7 \times 10^{-17}$ cm^2), which in turn is significantly lower than the total cross section for electronic excitation processes at 20 eV (see Itikawa, 2006).

Although energy transfer from suprathermal electrons to thermal electrons through Coulomb collisions represents an energy loss process for suprathermal electrons, we neglect these interactions, as the cooling process is not very efficient for suprathermal electrons with energies above 10 eV of interest here (e.g., Rees, 1989). We have finally neglected the energy loss associated with the momentum transfer from electrons to neutral molecules in elastic collisions, as this is predicted to be very small (e.g., Rees, 1989).

3.2.2. Comparison with a transport model

The simplified approach to calculate $P_{e,sec}(z)$ has been tested against results obtained with the more detailed method employed by Galand et al. (2010), which in contrast to the EED model also takes into account electron transport, electron–electron interactions and ro-vibrational excitation processes. The comparison between the models has been performed using the same cross-section sets (for ionization and electronic excitation processes), neutral density profiles, SZA values and impinging solar EUV spectrum corresponding to the T40 flyby. The model results do not deviate by more than 2% below 1200 km, so below this altitude it is clearly valid to use the simpler EED model. At higher altitudes larger differences are found. For example at 1270 km, the EED model provide an approximately 20% higher value than inferred from the model used by Galand et al. (2010). We attribute this difference to the lack of electron transport in the EED-model, in agreement with previous local approximation studies (Lavvas et al., 2011).

3.3. Remarks on the potential influence of non-solar ionization sources

Although non-solar ionization sources occasionally are important near dawn/dusk (Kliore et al., 2011) their contribution to the

total electron production rate is expected to be small for the considered low SZA dayside flybys. This can be argued for in two different ways. Let us first introduce P_S and P_{NS} to denote the electron production rates by solar and non-solar ionization processes, respectively. If we (1) neglect the possibility for dayside ions to survive into the nightside, (2) assume that the effective recombination coefficient is roughly similar on the dayside and the nightside, and (3) assume that $P_{NS}(\text{day}) = P_{NS}(\text{night})$ it follows that

$$P_S + P_{NS} = \alpha_{eff} \times (n_e(\text{day}))^2 \quad (6)$$

and

$$P_{NS} = \alpha_{eff} \times (n_e(\text{night}))^2 \quad (7)$$

Taking 5 as a typical ratio between dayside and nightside peak electron densities (Ågren et al., 2009) gives $P_{NS}/P_S \approx 0.04$. This ratio becomes smaller when taking into account the survival of dayside ions (and electrons assuming charge balance) into the nightside (Cui et al., 2009, 2010).

A second evidence for the small relative contribution of non-solar ionization sources on the dayside is based on suprathermal electron intensities measured by the ELectron Spectrometer (ELS), a subsystem of the CAssini Plasma Spectromer (CAPS) (see e.g. Coates et al., 2007). These intensities may be used in order to calculate the secondary electron production rate as proposed by Galand et al. (2010). The CAPS/ELS derived production rates presented by Galand et al. (2010) should, however, be increased by about a factor of 3 following the recent recalibration of the INMS instrument (see Section 2.2.1). For T40 near the ionospheric peaks at 1075 km (inbound) and 1060 km (outbound) the CAPS/ELS derived electron-impact electron production rates are then about 3 and 4 cm^{-3} s^{-1}, respectively, fairly similar to the solar-driven calculated values for $P_{e,sec}$ at the same altitudes and significantly smaller than the photoionization rates (see Section 5.1), showing that magnetospheric electron precipitation cannot have contributed significantly to the electron production rates in these sunlit cases.

4. Ion composition and estimates of the effective recombination coefficient in Titan's dayside ionosphere

In Fig. 6 dissociative recombination rate coefficients at $T_e = 300$ K derived from experiments at the heavy ion storage ring CRYRING (see e.g., Thomas, 2008; Larsson and Orel, 2008), are presented for 22 ions containing only hydrogen (or deuterium), carbon and nitrogen atoms, the main elements in Titan's atmosphere. We have also added the rate coefficient obtained by McLain et al. (2004) in a Flowing Afterglow Langmuir probe (FALP) experiment on the $C_2H_5^+$ ion and the rate coefficient for CH^+ derived from a storage ring experiment at TSR (Amitay et al., 1996; Sheehan and St-Maurice, 2004). Shown in Fig. 6 is also the best fit to a second order polynomial of the rate coefficients versus the number of atoms, V, in the molecular ions. The best fit for the dissociative recombination rate coefficient (in cm^3 s^{-1}) at $T_e = 300$ K is given by

$$\alpha_{300}(V) = (-0.0860 \times V^2 + 3.216 \times V - 4.878) \times 10^{-7} \quad (8)$$

Regarding the fully deuterated ions included in Fig. 6, experiments at CRYRING have occasionally shown strong isotopic effects in the dissociative recombination process with the fully deuterated ions having significantly lower reactivity than their hydrogenated analogues (see Vigren et al., 2010 and references therein). Noteworthy, however, McLain and Adams (2009) (FALP measurement) found a significantly lower rate coefficient for the dissociative recombination of CH_3CNH^+ than what Vigren et al. (2008) did for CD_3CND^+ (CRYRING measurement) (see Table 2).

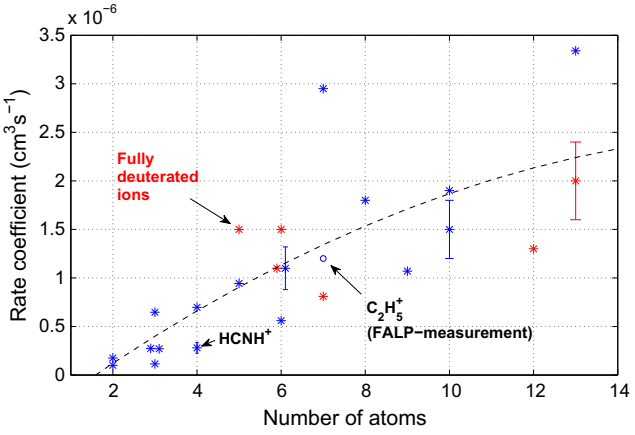

Fig. 6. Rate coefficients at an electron temperature of 300 K for the dissociative recombination of 23 ions on the form $C_xH_yN_z$ (blue) or $C_xD_yN_z$ (red) as measured at CRYRING and TSR (only CH^+) and the rate coefficient for the dissociative recombination of $C_2H_5^+$ (open circle) measured in a FALP experiment by McLain et al. (2004). The rate coefficients are plotted against the number of atoms in the different molecular ions. In a few cases the number of atoms in the molecular ions have been shifted by 0.1 in the plot as to better present all of the data. Uncertainties are generally quoted as 20%. The dashed black line is the best result from a fit of the data to a second order polynomial function, as given by Eq. (8). The plotted data points (going towards ions with an increasing number of atoms, and from lower to higher rate coefficients in each group of ions with a specific number of atoms) are associated with the following ions (with reference information): CH^+ (a), N_2^+ (b), H_3^+ (c), C_2H^+ (d), N_2H^+ (e), N_3^+ (f), $HCNH^+$ (g), CH_3^+ (h), NH_4^+ (i), $DCCCN^+$ (g), $C_2H_4^+$ (d), CH_5^+ (j), $C_4D_2^+$ (k), $DCCCND^+$ (g), CD_3CND^+ (g), $C_2H_5^+$ (l), $C_3H_4^+$ (l), CH_2CHCNH^+ (g), $C_3H_7^+$ (m), $(NH_3)_2H^+$ (n), $CH_3CH_2CNH^+$ (g), $C_6D_6^+$ (o), $C_6D_7^+$ (o), $(NH_3)_3H^+$ (n). References: (a) Amitay et al. (1996), Sheehan and St-Maurice (2004), (b) Peterson et al. (1998), (c) Sundström et al. (1994), (d) Ehlerding et al. (2004) (e) Vigren et al. (2012b), (f) Zhaunerchyk et al. (2007), (g) for references see Table 2 and Vigren et al. (2012a), (h) Thomas et al. (2012), (i) Öjekull et al. (2004), (j) Kaminska et al. (2010), (k) Danielsson et al. (2008), (l) McLain et al. (2004), (m) Ehlerding et al. (2003), (n) Öjekull et al. (2006), and (o) Hamberg et al. (2011). (For interpretation of the references to color in this figure legend, the reader is referred to the web version of this article.)

It appears from Fig. 6 that there is a trend of increasing rate coefficients with increased ion complexity. It has been speculated

Table 2
Dominant ions in Titan's upper atmosphere, their dissociative recombination rate coefficients at $T_e = 300$ K and their (dayside) average fractional abundances, f_{Dom}, (to the total INMS observed ion density) at an altitude of 1050 km, taken from Cui et al. (2009).

Ion	α_{300} (cm^3 s^{-1})	$100 \times f_{Dom}$ (1050 km)
CH_3^+	7.0×10^{-7} [a]	1.8
CH_5^+	1.1×10^{-6} [b]	1.5
$HCNH^+$	2.8×10^{-7} [c] (3.5×10^{-7} [d])	37.1
$C_2H_5^+$	1.2×10^{-6} [e]	8.5
$CH_2NH_2^+$	*1.1 × 10⁻⁶* [f]	2.2
$C_3H_3^+$	8.0×10^{-7} [g]	7.5
$C_3H_5^+$	*1.5 × 10⁻⁶* [f]	6.0
CH_3CNH^+	8.1×10^{-7} [h] (3.4×10^{-7} [d])	3.8
$HCCCNH^+$	1.5×10^{-6} [i]	8.5
CH_2CHCNH^+	1.8×10^{-6} [j]	3.9

[a] Thomas et al. (2012).
[b] Kaminska et al. (2010).
[c] Semaniak et al. (2001).
[d] McLain and Adams (2009).
[e] McLain et al. (2004).
[f] From Eq. (8).
[g] McLain et al. (2005) (we present here their result for the cyclic isomer).
[h] Vigren et al. (2008) (measurement done on CD_3CND^+).
[i] Geppert et al. (2004) (measurement done on $DCCCND^+$).
[j] Vigren et al. (2009).

that potential reasons for this experimentally observed trend may be that ions with more atoms (1) offer electron capture into a greater number of ro-vibrationally excited Rydberg states, acting as intermediate states in the indirect mechanism of the dissociative recombination process, and (2) also has a greater number of competing reaction channels accessible for the direct mechanism of dissociative recombination (e.g., Zhaunerchyk et al., 2008; Vigren et al., 2012a). It is stressed that the rate coefficients of several ions deviate significantly from the trend line depicted in Fig. 6 and that Eq. (8) should not be extended to even more complex molecular ions. In fact, judging only from Fig. 6 it seems as if the trend of increasing rate coefficients with increasing ion complexity stops as the number of atoms in the ions becomes higher than about 7. The highest α_{300} values ever measured for dissociative recombination reactions are in the vicinity of 4×10^{-6} cm^3 s^{-1}. Such high rate coefficients have been observed in FALP experiments on a few complex aromatic molecular ions such as $C_{16}H_{10}^+$ and $C_6H_{13}^+$ (Novotny et al., 2005; Osborne et al., 2011), but there are also ions of similar complexity with reported α_{300} values below 10^{-6} cm^3 s^{-1} (e.g., Osborne et al., 2011).

$HCNH^+$ is the dominant ion in Titan's upper atmosphere in the 1050–1200 km altitude range (e.g., Vuitton et al., 2006, 2007; Westlake et al., 2012; Cravens et al., 2006; Cui et al., 2009). At 1150 km (1050 km) it accounts for about 50% (40%) of the ion population detectable by the INMS instrument in its OSI mode, which is limited to ions with a maximum mass-to-charge ratio of 99 Daltons (Westlake et al., 2012; Cui et al., 2009). Moreover, at 1050 km, the ions with mass-to-charge ratios of 15, 17, 28, 29, 30, 39, 41, 42, 52 and 54 Daltons account in total for about 80% of the INMS/OSI observed ion population (Cui et al., 2009). The $HCNH^+$ fraction and the fraction of dominant ions at 1050 km, appear to be similar to that presented by Westlake et al. (2012) for the inbound leg of T40 at 1079 km. The ions with mass-to-charge-ratios of 15, 17, 28, 29, 30, 39, 41, 42, 52 and 54 Daltons have been attributed to CH_3^+, CH_5^+, $HCNH^+$, $C_2H_5^+$, $CH_2NH_2^+$, $C_3H_3^+$ (predominantly the circular isomer), $C_3H_5^+$, CH_3CNH^+, $HCCCNH^+$ and CH_2CHCNH^+, respectively (Vuitton et al., 2006, 2007). The dissociative recombination rate coefficients determined experimentally at T_e = 300 K for these ions are listed in Table 2, alongside their dayside average fractional abundances at 1050 km taken from the work by Cui et al. (2009). Note that for $CH_2NH_2^+$ and $C_3H_5^+$ we have not found rate coefficients in the literature, so the rate coefficients for these ions have been set based on Eq. (8).

The ion composition is anticipated to change when going towards higher altitudes. It is expected that the total fractional abundance of the 10 dominant ions should be higher at 1200 km than at 1050 km. Westlake et al. (2012) reported that for T40, at altitudes close to 1150 km, $HCNH^+$, $C_2H_5^+$ and CH_5^+ make up about 50%, 14% and 2%, respectively, of the ion signal measured by the INMS.

Based on the works by Crary et al. (2009) and Wahlund et al. (2009) we deem it unlikely that heavy ions (with masses above 100 amu) account for significantly more than 10% (and probably only a few per cent) of the ion population above 1050 km. It then follows that Eq. (9) below should give a good estimate of $\alpha_{eff,300}$, at least above 1050 km

$$\alpha_{eff,300}(z) = \left(1 - \sum_{Dom} f_{Dom}(z)\right) \times \alpha_{x,300}(z) + \sum_{Dom} \alpha_{Dom,300} f_{Dom}(z) \qquad (9)$$

Summations are made over the 10 dominant ion species (*Dom*) in Table 2, f_{Dom} is the fraction of ion species *Dom* to the total ion density measured by the INMS, $\alpha_{Dom,300}$ is the rate coefficient at T_e = 300 K for the dissociative recombination of the ion species *Dom* and $\alpha_{x,300}$ is the average recombination coefficient among the non-dominating ions. Using the rate coefficients and f_{Dom} values listed in Table 2 and using as a low estimate of $\alpha_{x,300}$, 1.0×10^{-6} cm^3 s^{-1} results in $\alpha_{eff,300} = 8.3 \times 10^{-7}$ cm^3 s^{-1}. Increasing $\alpha_{x,300}$ to a high estimate of 2.5×10^{-6} cm^3 s^{-1} gives $\alpha_{eff,300} = 1.14 \times 10^{-6}$ cm^3 s^{-1}.

The $\alpha_{eff,300}$ values calculated above were retrieved based on fractional ion abundances at 1050 km. Similar calculations using fractional abundances obtained above 1100 km results in somewhat lower values, due to increased fractional abundances of $HCNH^+$, which has a low rate coefficient for dissociative recombination. A very simplified estimate of $\alpha_{eff,300}$ at 1200 km is achieved by setting the fractional abundance of $HCNH^+$ to 50%. By the assumption that the remainder of the ions have an average rate coefficient between 1.0×10^{-6} and 1.5×10^{-6} cm^3 s^{-1} (which is reasonable from the rate coefficients listed in Table 2) we obtain "low" and "high" $\alpha_{eff,300}$ estimates of 6.4 and 8.9×10^{-7} cm^3 s^{-1}, respectively. We therefore propose the following linear relation as a high estimate of $\alpha_{eff,300}(z)$ for $1050 < z < 1200$ km

$$\alpha_{eff,300,High}(z) = 2.890 \times 10^{-6} - 1.667 \times 10^{-9} \times z \qquad (10)$$

while the low prediction of $\alpha_{eff,300}(z)$ is approximately 28% lower, i.e.

$$\alpha_{eff,300,Low}(z) = 0.72 \times \alpha_{eff,300,High}(z) \qquad (11)$$

In Fig. 7 these functions are plotted and extended downwards to 1000 km, though it is noted that below 1050 and in particular near 1000 km the estimates are highly uncertain due to the possibility of significant abundances of heavy (>100 amu) ions (Crary et al., 2009) and the limited knowledge on their rate coefficients for dissociative recombination reactions. For this reason and because of the increased abundances of negative ions near 1000 km in Titan's ionosphere (Coates et al., 2007) we consider in particular altitudes between 1050 and 1200 km in our comparisons of predicted and observed electron number densities addressed in Section 5.2. We note finally that Galand et al. (2010) presented values of $\alpha_{eff,500}$ based on INMS ion density measurement and the reaction list of Vuitton et al. (2007). When these values are converted to their corresponding $\alpha_{eff,300}$ values they agree to within 10% with our low estimate of $\alpha_{eff,300}$ (Eq. (11)) throughout the considered altitude range.

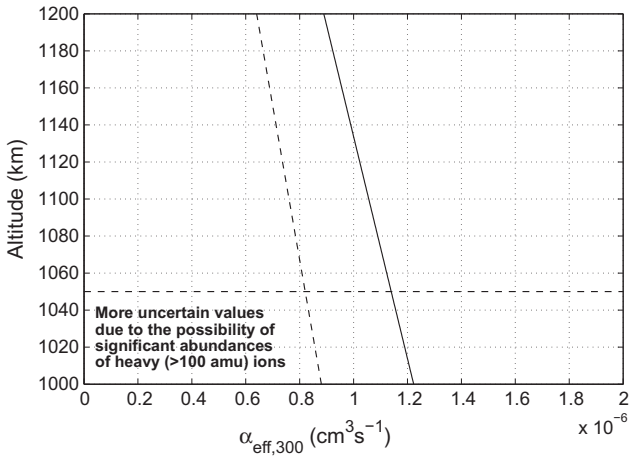

Fig. 7. High (solid black line) and low (dashed black line) predictions of $\alpha_{eff,300}$ as a function of altitude in Titan's upper atmosphere (see Eqs. (10) and (11)). The predictions below 1050 km are highly uncertain due to the increased relative abundances of heavy (>100 amu) ions for which there is a limited knowledge regarding their rate coefficients for dissociative recombination reactions.

5. Results and discussion

5.1. Comparison of peak altitudes for observed n_e and calculated P_e

Fig. 8 shows the secondary and total electron production rates, $P_{e,\mathrm{sec}}(z)$ and $P_e(z)$, calculated using the model described in Section 3, versus altitude along the Cassini trajectory for the T40, T41, T42 and T48 Titan flybys below 1200 km.

Note that the only considered source of energy is solar radiation. Auroral electron precipitation has been neglected in the calculations of P_e (see Section 3.3). It is seen that for the considered altitude and SZA regions, $P_{e,\mathrm{sec}}(z)$ gives a small contribution (typically less than 25%) to $P_e(z)$, which is dominated by $P_{e,\mathrm{prim}}(z)$. The N_2 photoionization cross-section is lower for soft X-rays compared with EUV photons. This implies that the relative contribution to $P_e(z)$ from the secondary electron production rate is expected to increase with decreasing altitude and increasing SZA. As shown in Table 3, the maximum electron production rates are located near altitudes corresponding to the unit optical depth for HeII photons of wavelength 30.38 nm, the strongest solar line in the EUV spectra (see Fig. 5).

Changing neutral densities within 20% has a small influence on the displayed P_e profiles. Increased (decreased) neutral densities by 20% shift the predicted peak altitudes of the electron production rates upwards (downwards) by maximum 10 km. Fig. 8 also shows that: (1) The highest P_e values are associated with the T41 flyby. P_e depends both on the attenuated flux and the ambient density of N_2 and CH_4. The integrated incident solar EUV flux was roughly similar to the days corresponding to the T40 and T42 flybys. In Fig. 2 it is seen, however, that the N_2 densities observed at high altitudes during the T41 flyby are lower than the N_2 densities observed for the other flybys (causing less absorption of the solar flux), while at lower altitudes the N_2 densities are comparable to the other flybys. (2) The P_e profile for the inbound leg of T48 sticks out because of a marked change in the N_2 density profile around 1050 km. (3) The P_e values at 1030 and 1020 km for the inbound leg of T40 are nearly similar as a combined result of decreasing SZA, decreased deposition of EUV photons and increased deposition of X-rays yielding the production of energetic photoelectrons.

Table 3
N_2 column densities, C_{peak}, in the line of sight towards the Sun at the positions of maximum electron production rates, and the corresponding optical depths, τ, for HeII photons at 30.38 nm.

Ion	C_{peak} ($10^{16} \times \mathrm{cm}^{-2}$)	τ
T40 (inbound)	7.37	0.86
T40 (outbound)	6.73	0.78
T41 (inbound)	8.77	1.02
T41 (outbound)	6.82	0.79
T42 (inbound)	10.45	1.21
T42 (outbound)	8.49	0.98
T48 (inbound)	8.81	1.02
T48 (outbound)	7.55	0.88

Note: The optical depths are here calculated as $\tau = C_{peak} \times \sigma(N_2, 30.38)$ with $\sigma(N_2, 30.38) = 11.60 \times 10^{-18}\ \mathrm{cm}^2$ being the photoionization (=photoabsorption) cross section of N_2 for photons of wavelength 30.38 nm.

Fig. 9 shows the altitudes where the electron production rates are calculated to peak and where the electron number densities are observed to peak during the different flybys. The assignment of n_e peak altitudes is mainly based on high-time resolution LP measurements and the error bars have been set manually to assure that the possible peak altitudes are included for each flyby. The data for T40, T41 and T42 have been published previously in Ågren et al. (2009). It is noted, however, that re-analysis of the T42 flyby shows that the peak altitude for the outbound leg should be revised upwards by about 33 km from what was presented in Fig. 7 of that work (for the inbound part of T42 only the error margins of the altitude of maximum n_e have been changed compared with Fig 7. of Ågren et al. (2009)).

As illustrated in Fig. 8 for T40, previously the altitudes of maximum electron production rates were predicted at significantly lower altitudes (Galand et al., 2010). The neutral density profiles, updated in this work with respect to those previously used, such as by Galand et al. (2010) (see Section 2.2.1), bring an improved agreement between the peak altitudes of the electron production rates and the electron densities. The increased densities shift the peak of electron production upward, since for a given SZA the attenuation of the solar flux at a given altitude is larger.

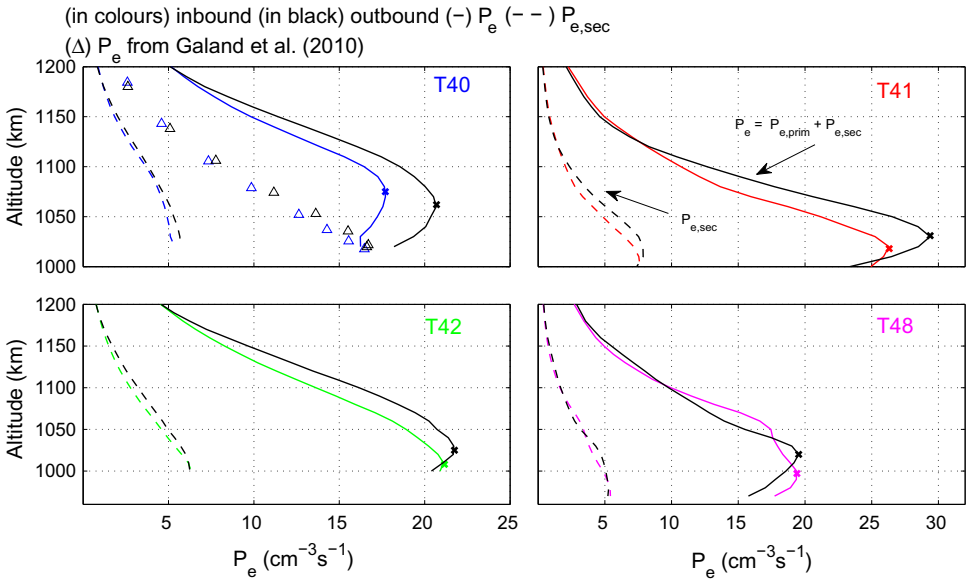

Fig. 8. Calculated (total) electron production rates (solid lines) and secondary electron production rates (dashed lines), for the inbound (colored) and outbound (black) parts of the T40 (blue), T41 (red), T42 (green) and T48 (magenta) flybys. The bold crosses (×) are located where the total electron production rates peak. The triangles (Δ) are the total electron production rates presented by Galand et al. (2010) for the T40 flyby. (For interpretation of the references to color in this figure legend, the reader is referred to the web version of this article.)

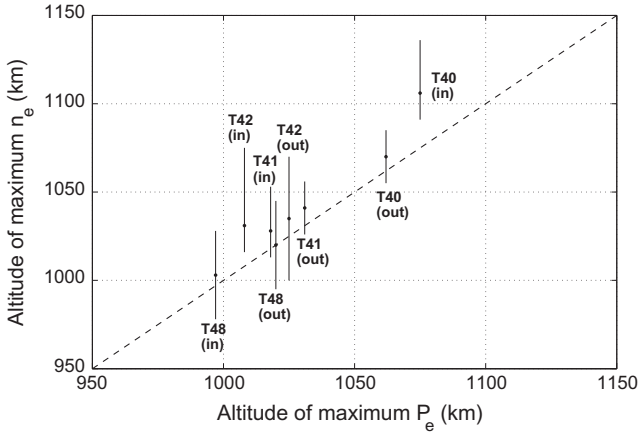

Fig. 9. Comparison between the altitudes of maximum P_e (calculated) and maximum n_e (observed). A bold point at the dashed diagonal line implies that the altitudes of maximum n_e and maximum P_e coincide.

As shown in Fig. 9, in addition to T40 the electron densities observed during T41, T42 and T48 also tend to peak near the same altitudes as the peak electron production rates, although it is noted that in some cases the assigning of a peak altitude for the electron density is ambiguous due to somewhat flat density profiles near the peak. The improved agreement between the peak altitudes of P_e and n_e confirms earlier findings. Using T18 data, before the recent INMS neutral density correction was announced, Robertson et al. (2009) showed that increased neutral densities (factor of 2.5) would yield an improved agreement between the peak altitudes of the LP-derived electron densities and the corresponding peak altitudes predicted by their solar-driven ionization model. We note from Fig. 9 that there is still some disagreement between the peak altitudes of n_e and P_e; the n_e values tend to peak a few km higher up than P_e. This may suggest that the neutral densities still are somewhat underestimated, though it is noted that n_e does not only relate to P_e, so the peaks of n_e and P_e do not necessarily have to coincide. As for the inbound part of T40, where we observe the largest discrepancy between the peak altitudes of n_e and P_e, the calculated P_e at 1090 km and 1100 km are only about 2% and 7% lower than the maximum P_e value found at 1075 km. From Eq. (3) it is then realized that in order to reach the same n_e values at 1090 (1100) km as at 1075 km requires only the α_{eff} value at 1090 (1100) km to be 2% (7%) lower than at 1075 km. Such small changes of α_{eff} may be expected over a distance of 15 (25) km due to small variations in the electron temperature and in the ionic population. In addition it is noted that we have neglected some features, which could slightly affect the peak altitudes of n_e and P_e, e.g., negative ions (their formation and destruction routes) and non-solar ionization sources.

Our assumptions of photochemical equilibrium and loss of electrons exclusively by dissociative recombination with $T_e^{-0.7}$ dependencies of the rate coefficients is expected to result in nearly linear relations between $P_e(T_e/300)^{0.7}$ and n_e^2, should there not be large variations in the $\alpha_{eff,300}$ values. For points below 1100 km associated with the T40 flyby we have studied how the ratio $P_e(T_e/300)^{0.7}/n_e^2$ changes with employed neutral densities. The results of these calculations are shown in Fig. 10. It can be seen that the density profiles used in this work result in $P_e(T_e/300)^{0.7}$ values, that are linearly related to n_e^2 while decreasing or increasing the neutral densities by 33% result in more scattered data as $P_e(T_e/300)^{0.7}$ is plotted against n_e^2. Though we highlighted uncertainties in the effective recombination coefficient below 1050 km in Section 4, the linear relation between $P_e(T_e/300)^{0.7}$ and n_e^2 shown in the mid panel of Fig. 10 seems to suggest a roughly constant value of $\alpha_{eff,300}$ for altitudes between 1020 and 1100 km associated with the T40 flyby (at higher altitudes the value of $\alpha_{eff,300}$ reduces due to compositional changes as further illustrated in Section 5.5). Note however that the ratios of $P_e(T_e/300)^{0.7}/n_e^2$ are significantly higher (roughly a factor of 4) than expected from our predictions of $\alpha_{eff,300}$ which may point towards systematic errors in input parameters or missing electron loss processes (these points are expanded upon in Sections 5.2–5.5).

5.2. Comparison of observed and predicted electron number densities

Table 4 gives predicted and observed electron number densities for the T40, T41, T42 and T48 Titan flybys between 1050 and 1200 km. The predicted $n_{e,Model}$ values are based on Eq. (5) using T_e measurements from the LP (sweep mode), the electron production rates shown in Fig. 8 and the estimates of $\alpha_{eff,300}(z)$ given by Eq. (10). Using the high estimate of $\alpha_{eff,300}(z)$, as we did to compute the values of Table 4, results in lower n_e predictions but it is still seen that even these lower estimates of the electron densities are about a factor of 1.5–2 higher than the observed n_e. There is a weak overall trend of increased relative discrepancy between predicted and observed n_e values towards lower altitudes, though the inbound part of T41 display an opposite behavior.

In Fig. 1 we show $n_{e,Model}$ values ranging from the altitude of the closest approach up to 1400 km for the inbound legs of T40, T41 and T42 and for the outbound leg of T48. These are the flyby parts for which the LP-derived electron temperatures may be best fitted to second order polynomial functions as seen in Fig. 4. For the model values in Fig. 1 we have used Eq. (10) as values of $\alpha_{eff,300}(z)$ in between 1050 km and 1200 km. Below 1050 km and above 1200 km we use constant values of $\alpha_{eff,300}(z)$ equal to the values given by Eq. (10) at 1050 km and 1200 km, respectively. Note that the $n_{e,Model}$ values shown by dashed lines in Fig. 1 have been divided by a factor of 2 to illustrate the fact that our model captures the observed electron number density reasonably well in a relative sense. It is stressed that above 1200 km, or at least above 1300 km, we anticipate transport effects to play an important role for the electron balance. Moreover the use of a constant value of $\alpha_{eff,300}(z)$ above 1200 km may certainly be questioned. It is in fact likely, judging from Figs. 8 and 9 in Cui et al. (2009) and the laboratory derived rate coefficients for the dissociative recombination of e.g., CH_5^+, $HCNH^+$ and $C_2H_5^+$, that $\alpha_{eff,300}(z)$ may have a "local" minimum value somewhere in the altitude range between 1200 and 1400 km as suggested by Galand et al. (2010). Nevertheless, should the $\alpha_{eff,300}$ value at some points between 1200 and 1400 km be say 25% lower (higher) than the selected constant value, the corresponding $n_{e,Model}$ value would increase (decrease) only by about 15% (10%). In addition the use of a constant $\alpha_{eff,300}$ below 1050 km, where the relative abundance of heavy, complex ions may reach high values, could be questioned. We use a constant value mainly based on the linear relationships seen between $P_e(T_e/300)^{0.7}$ and the square of observed electron number densities (illustrated for T40 in Fig. 10). In addition, by instead extending Eq. (10) to z = 1000 km the $\alpha_{eff,300}$ value at 1000 km only becomes about 7% higher than the constant value used to produce the $n_{e,Model}$ values in Fig. 1.

The discrepancy between n_e predictions and n_e observations in Titan's sunlit ionosphere becomes even more pronounced in light of the fact that we have not taken into account non-solar ionization sources when calculating $n_{e,Model}$ values based on Eq. (5). The addition of e.g., ionization caused by magnetospheric electrons, would increase the total electron production rates and thereby increase the predicted n_e values making the agreement with the observed n_e values even worse. However, as shown in Section 3.3, we anticipate non-solar ionization sources to contribute with less than about 5% to the total electron production rates.

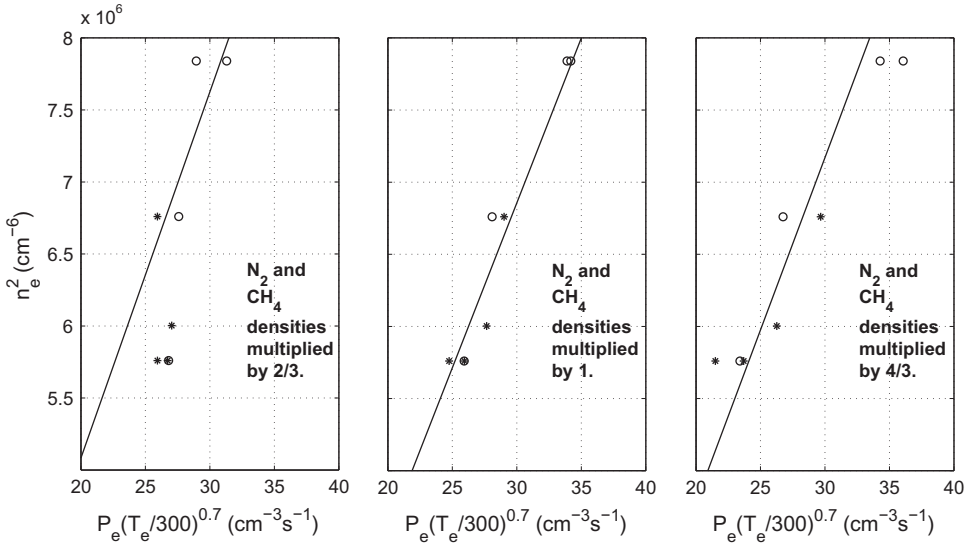

Fig. 10. n_e^2 (Observed) versus $P_e(T_e/300)^{0.7}$ (calculated/observed) for inbound (asterisks) and outbound (open circles) points below 1100 km during the T40 flyby. The points in the middle panel correspond to the P_e values calculated with the updated density profiles that is primarily used in this work. The points in the left and the right panels correspond to P_e values calculated with 33% lower and higher neutral densities, respectively. The solid lines show the best linear fits of the data fulfilling that $P_e = 0$ cm^{-3} s^{-1} gives $n_e = 0$ cm^{-3}.

Table 4
Ratio, R, between predicted (Eq. (5)) and observed electron number densities for heights between 1050 and 1200 km for the T40, T41, T42 and T48 Titan flybys. We have used $\alpha_{eff,300}(z)$ according to Eq. (10). Values in parentheses are solar zenith angles in degrees. Multiplying the values in brackets by 10^3 gives measured electron number densities in cm^{-3}. The mean of the R-values in the left-hand side of the table is 1.75, whereas it is 1.90 in the right-hand side (lower altitudes).

z (km) (SZA in °)	Flyby	R (n_e in 10^3 cm^{-3})	z (km) (SZA in °)	Flyby	R (n_e in 10^3 cm^{-3})
1185 (55)	T40(in)	1.86 [1.94]	1107 (26)	T40(out)	1.96 [2.75]
1181 (19)	T48(in)	1.50 [1.88]	1106 (50)	T40(in)	1.85 [2.70]
1181 (22)	T40(out)	1.86 [1.95]	1103 (19)	T41(out)	1.85 [2.40]
1180 (11)	T42(out)	1.64 [1.98]	1101 (12)	T42(out)	1.95 [2.31]
1167 (40)	T48(out)	1.62 [1.90]	1088 (33)	T42(in)	1.83 [2.44]
1159 (46)	T41(in)	2.07 [1.44]	1084 (36)	T48(out)	1.89 [2.17]
1159 (37)	T42(in)	1.74 [2.12]	1084 (42)	T41(in)	1.59 [2.87]
1144 (52)	T40(in)	1.72 [2.40]	1079 (48)	T40(in)	1.98 [2.60]
1140 (11)	T42(out)	1.99 [2.02]	1075 (28)	T40(out)	1.98 [2.80]
1139 (24)	T40(out)	1.90 [2.45]	1072 (13)	T42(out)	1.88 [2.67]
1138 (18)	T41(out)	1.87 [1.72]	1068 (21)	T41(out)	1.98 [2.95]
1135 (19)	T48(in)	1.47 [2.38]	1059 (20)	T48(in)	1.93 [2.43]
1126 (38)	T48(out)	1.59 [2.42]	1057 (31)	T42(in)	1.79 [2.91]
1122 (35)	T42(in)	1.79 [2.48]	1053 (30)	T40(out)	1.96 [2.80]
1121 (44)	T41(in)	1.64 [2.32]	1052 (46)	T40(in)	2.01 [2.45]

5.3. Results from Cassini Titan dayside flybys at different geometric conditions

We have so far focused on four Titan dayside flybys with similar geometrical conditions. Here we extend the investigation to the outbound legs of the T36 (October 2, 2007, SLT = 11.49 h, C/A = 973 km) and T39 (December 20, 2007, SLT = 11.36 h, C/A = 970 km) Titan flybys and to the T43 (May 12, 2008, SLT = 10.99 h, C/A = 1001 km) flyby. Geometrical data for these flybys are presented in Table 5 alongside information on INMS derived N_2 and CH_4 number densities and LP-derived electron temperatures. Though the longitudes overlap with those from our earlier flyby set, T36 and T39 occurred at significantly larger latitudes in the southern hemisphere. Also the SZA during these outbound legs are generally larger than the ones associated with the T40, T41, T42 and T48 flybys below 1200 km, but still we believe they are low enough for solar-driven ionization sources to largely dominate as a contributor to the electron production rates. In contrast to the other investigated flybys the T43 flyby occurred in Titan's northern hemisphere.

The incident solar fluxes on the days corresponding to the T36, T39 and T43 flybys were all fairly similar to the day corresponding to the T40 flyby (see Fig. 5). In Section 3.1 we defined F_X as the integrated flux below X nm and it is noted that F_{80}(T40)/F_{80}(T36), F_{80}(T40)/F_{80}(T39) and F_{80}(T40)/F_{80}(T43) were 1.12, 1.01 and 1.04, respectively. The calculated peak electron production rate for T36 outbound (T39 outbound) occurs at 1058 (1075) km with a value of 12.7 (17.6) cm^{-3} s^{-1}. For T43 inbound (outbound) P_e peaks at an altitude of 1029 (1025) km with a value of 20.6 (23.9) cm^{-3} s^{-1}. The altitudes of maximum electron production rates match the peak altitudes of the observed electron densities well (T36 outbound: 1050 km, T39 outbound: 1082 km, T43 inbound: 1051 km, T43 outbound: 1002 km) as were also the case in the T40, T41, T42 and T48 studies.

To produce the $n_{e,Model}$ graphs seen in Fig. 11 we used as T_e best-fit-functions of the LP-derived T_e values as a function of altitude. Similar as when producing the graphs in Fig. 1 we used $\alpha_{eff,300}(z)$ values according to Eq. (10) in between 1050 and 1200 km, and with constant values below and above these limits. As seen in Fig. 11 the over-prediction of the calculated electron number

Table 5
Geometric data, INMS derived density data and LP-derived electron temperatures for the T36 (outbound), T39 (outbound) and T43 Titan flybys at closest approach and at 1200 km.

Flyby	SZA (°)	Lat. (°)	Long. (°)	$n(N_2)$ (cm^{-3})	$n(CH_4)$ (cm^{-3})	T_e (K)
T36 (C/A, 973 km)	67	60S	109	2.3(10)[a]	2.6(8)	500[b]
T36 (out, 1200 km)	48	54S	147	9.6(8)	3.6(7)	750
T39 (C/A, 970 km)	61	70S	177	2.8(10)	3.9(8)	550
T39 (out, 1200 km)	47	51S	194	7.2(8)	2.4(7)	800
T43 (in, 1200 km)	45	8 N	120	5.2(8)	1.6(7)	700
T43 (C/A, 1001 km)	36	18 N	137	1.5(10)	2.3(8)	300
T43 (out, 1200 km)	35	27 N	155	3.3(8)	1.1(7)	500

[a] 2.3(10) should be read as 2.3×10^{10}.
[b] The given electron temperatures are estimates based on LP measurements (sweep mode) near the specified altitudes.

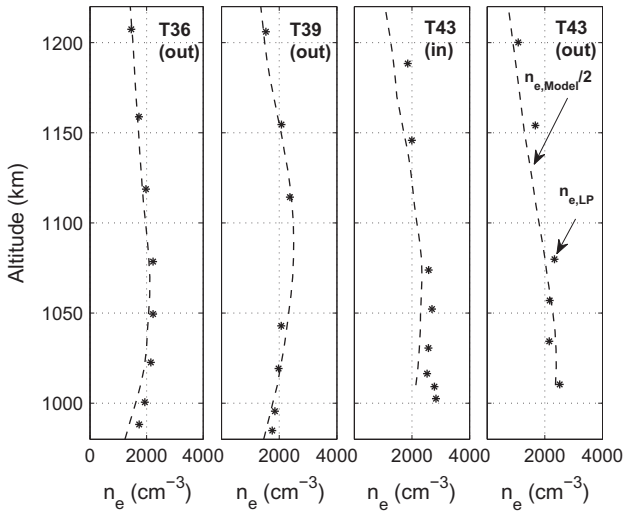

Fig. 11. LP-derived electron number densities (asterisks) and model derived values divided by 2 (dashed lines) versus altitude for the T36 (outbound), T39 (outbound) and T43 (inbound + outbound) Titan flybys by the Cassini spacecraft. The modeled values are based on Eq. (5) with P_e calculated as described in Section 3, T_e being taken from the fits of the LP-derived T_e-data and with $\alpha_{eff,300}$ treated as constant above 1200 km and below 1050 km, and according to Eq. (10) in between 1050 and 1200 km.

densities compared with those observed prevails for these flybys as well. In particular near the ionization peak our predicted n_e values are about a factor of 2 higher than observed. Note also that we have used here the high estimate of $\alpha_{eff,300}(z)$ yielding lower estimates of n_e.

5.4. Potential reasons for the discrepancy between observed and predicted electron number densities in Titan's sunlit upper atmosphere

There may be different reasons as to why our predicted $n_{e,Model}$ values are higher than the observed $n_{e,LP}$ values. Here we discuss briefly (1) the LP measurements of n_e, (2) the sensitivity of $n_{e,Model}$ to the different input parameters of Eq. (5) and (3) the possibility that we may be missing in our calculations important loss processes of thermal electrons.

5.4.1. Uncertainties in n_e observation

The uncertainties in the n_e measurements by the LP are anticipated to be less than 10% (Wahlund et al., 2009; Ågren et al., 2009). Significant systematic errors, for example due to spacecraft shadowing of the LP (as discussed by Laframboise and Godard, 1974 for the Explorer 31 satellite) are unlikely as LP derived electron number densities have been confirmed by an independent measurement technique in which n_e is calculated based on the upper hybrid emission line as obtained by the Wideband Receiver (WBR) on the RPWS (see e.g., Wahlund et al., 2009). In addition, the electron number densities inferred from radio occultation measurements are generally matching those observed by the LP near dawn/dusk (see Kliore et al., 2011; Galand et al., 2013). Moreover, at high altitudes (where the number density of ions heavier than 100 amu is low, typically above ~1100 km) the LP derived electron number densities agree reasonably well with the total ion densities inferred from INMS/OSI measurements (Robertson et al., 2009; Wahlund et al., 2009).

5.4.2. Sensitivity of calculated n_e to input parameters

Table 6 summarizes the outcome of sensitivity tests on $n_{e,Model}(z)$ by varying the physical quantities β, P_e (for this we study the effect of changing neutral densities and the solar spectral irradiance impinging on the atmosphere), T_e and $\alpha_{eff,300}(z)$ used to calculate $n_{e,Model}(z)$ via Eq. (5).

5.4.2.1. β Sensitivity. Using $\beta = -0.7$ in the calculations appears as a reasonable choice given the electron temperature dependencies observed in laboratory experiments of dissociative recombination reactions (e.g., Vuitton et al., 2007). As examples the CRYRING measurements of CH_3^+, CH_5^+, $HCNH^+$, CD_3CND^+, $DCCCND^+$ and CH_2CHCNH^+ revealed temperature dependencies of $T_e^{-0.70}$, $T_e^{-0.72}$, $T_e^{-0.65}$, $T_e^{-0.69}$, $T_e^{-0.58}$ and $T_e^{-0.80}$, respectively (for references see Table 2). In the sensitivity test we have studied the effect on $n_{e,Model}(z)$ of using $\beta = -0.5$ and -0.9, as the vast majority of measured β values falls within this range. Using $\beta = -0.5$ decreases the values of $n_{e,Model}$ by about 8% at 1200 km and somewhat less at lower altitudes where T_e is lower, while using $\beta = -0.9$ increases the $n_{e,Model}$ values in similar proportions.

5.4.2.2. P_e sensitivity. We note first that a 20% decrease of a P_e value only decreases the corresponding $n_{e,Model}$ value by 10% due to the square root relation in Eq. (5). $P_e(z)$ is a function of several physical quantities, namely the solar spectral irradiance at the top of the atmosphere, the neutral density profiles and the photo-absorption (ionization) cross sections. As seen in Fig. 8 $P_{e,sec}(z)$ gives only a small contribution to $P_e(z)$, such that a small change in $P_{e,sec}(z)$ yields a much smaller change in $P_e(z)$ and $n_{e,Model}(z)$.

If the spectral irradiance is increased (decreased) uniformly over the whole spectrum the $P_e(z)$ values increase (decrease) with the same percentage due to the proportionality in the Beer–Lambert law. Varying the intensities in each of the different wavelength intervals in a stochastic manner may lead to small changes in the $P_e(z)$ profile, but we have not performed such tests as our prime goal with the sensitivity tests is to see whether the values of $n_{e,Model}(z)$ may be significantly reduced following a systematic error in some input variable. It is noted that the uncertainties in the spectral range below 27 nm is somewhat higher than at longer wavelengths (see Section 3.1). These photons are, however,

Table 6
Effects on the calculated values of $n_{e,Model}$ at 1200 and 1050 km following the specified changes in input parameters. Each one of the "actions" listed below the dashed horizontal line affect the $n_{e,Model}$ values in a similar way regardless of altitude.

Action	Effect on $n_{e,Model}$ at z = 1200 km	Effect on $n_{e,Model}$ at z = 1050 km
$\beta = -0.5$	Decrease by ~8%	Decrease by ~5%
$\beta = -0.9$	Increase by ~9%	Increase by ~5%
$n(N_2)$ and $n(CH_4)$ increased by 20%	Increase by ~8–10%	Increase by ~0–5%
$n(N_2)$ and $n(CH_4)$ decreased by 20%	Decrease by ~8–10%	Decrease by ~0–5%
Impinging EUV-flux changed by ±20%	Change by ~±10%	Change by ~±10%
T_e decreased by 20%	Decrease by ~8%	Decrease by ~8%
$\alpha_{eff,300,High}$ (see Eq. (10)) increased by 30%	Decrease by ~12%	Decrease by ~12%

due to their low N_2 and CH_4 photoabsorption cross sections, expected to mainly be absorbed below 1000 km.

Effect of changes in the $N_2(z)$ and $CH_4(z)$ densities by ±20% on $P_e(z)$ (and thereby $n_{e,Model}(z)$) varies with altitudes (see Section 5.1 for a discussion on the effect on the altitudes of the peak electron production rates) as P_e depends both on the attenuated flux and the ambient atmospheric densities.

The laboratory data of cross sections for photoabsorption/ionization processes are generally stated to be accurate within 20%. As there is no reason to assume that the cross sections that have been used for the different photo-processes are systematically lower (or higher) than the true values, we have not performed sensitivity tests of these parameters.

5.4.2.3. T_e sensitivity. Richard et al. (2011), focusing in particular on the T18 dayside flyby, calculated the electron temperatures in Titan's upper atmosphere by solving the energy equation for thermal electrons. Depending on the magnetic topology they considered, they obtained different levels of agreement with the LP derived electron temperatures (the fact that T_e is highly sensitive to the magnetic field has also been shown in previous studies, e.g., Galand et al., 2006; Roboz and Nagy, 1994). T_e estimates near 1050 km and below were generally, regardless of the magnetic topology, close to the neutral temperature values (150–170 K), i.e. severely lower than the T_e values inferred from the LP measurements (400–500 K), though the LP is sensitive enough to measure electron temperatures below 400 K (see e.g., Galand et al., 2013). On the one hand it can be speculated that an additional source of heating could be missing in the calculations. On the other hand instrumental properties make the LP measurement of low electron temperatures (below 300 K) difficult. Above about 1050 km and up to 1300 km (see Figs. 9 and 10 in Richard et al. (2011)) the agreement between calculated and observed T_e was found to depend on the considered magnetic topology, with differences up to a factor of 2. Reducing T_e by such a factor while keeping the other variables fixed, yields a decrease of $n_{e,Model}(z)$ by about 22%. A less drastic decrease of the T_e values, by 20%, reduces the $n_{e,Model}(z)$ values by about 8%.

5.4.2.4. $\alpha_{eff,300}$ Sensitivity. In Section 4, we introduced Eq. (10) as an upper limit of $\alpha_{eff,300}(z)$. In this section we explore hypothetical scenarios that act to further increase this upper limit, thereby further reducing the low predictions of $n_{e,Model}(z)$ values.

As a first sensitivity check we have tested how the high prediction of $\alpha_{eff,300}$ at 1050 km is affected by the assumption that heavy ions (with masses above 100 amu) account for 10% (20%) of the ion population, and that they have a very high average rate coefficient for dissociative recombination of 4×10^{-6} cm^3 s^{-1} at T_e = 300 K. These assumptions increase the previously determined upper limit of $\alpha_{eff,300}$ at 1050 km by 25% (50%) and decrease the $n_{e,Model}$ values at 1050 km by 10% (18%). At altitudes higher than 1100 km, assumptions of such high fractional abundances of heavy ions cannot be justified judging from Fig. 8 in Crary et al. (2009). It is also reminded that the dissociative recombination of several heavy molecular ions have been observed to have rate coefficients in the vicinity of (and even lower than) 1×10^{-6} cm^3 s^{-1} at T_e = 300 K (Osborne et al., 2011).

Recombination rate coefficients depend not only on the electron temperature but also the ion temperature (internal excitation). Ion temperatures derived in Titan's upper atmosphere (Crary et al., 2009) are in reasonable agreement with the ion temperatures predicted by Richard et al. (2011). These studies suggest that below 1200 km the kinetic ion temperature is close to the neutral temperature of about 150–170 K (see Fig. 11 in Richard et al. (2011)). Assuming that the rotational temperature of the ions, T_{rot}, is similar to the kinetic temperatures raises the question on how T_{rot} may influence the rate coefficient for dissociative recombination.

From their FALP experiment, McLain and Adams (2009) reported a temperature dependence of $T^{-1.38}$ for the rate coefficient of the dissociative recombination of $HCNH^+$. In comparing their result with the electron temperature dependence reported from the CRYRING experiment by Semaniak et al. (2001), namely $T_e^{-0.65}$, they argued that the significant difference in temperature dependence may be associated with the fact that while T_e is expected to be equal to the internal temperature of the ions in the FALP experiment, that is not the case in the storage ring experiments, such as those conducted at CRYRING. In the latter type of experiment, the method of ion production combined with a sufficiently long storage time allowing for radiative cooling, leads in the ideal case to dissociative recombination measurements of ions with T_{rot} close to 300 K. Accordingly, McLain and Adams (2009) argued that the rate coefficient for the dissociative recombination of $HCNH^+$ depends both on the electron temperature and the ion temperature (T_j), and suggested power law dependencies of $T_e^{-0.65}$ and $T_j^{-0.73}$ to reach consistency between the two approaches. This is an interesting hypothesis and as McLain and Adams (2009) point out, theoretical calculations to further study ion temperature dependencies for dissociative recombination reactions would be very valuable (in particular for $HCNH^+$). Accounting for a power law dependence of the ion temperature modifies Eq. (5) according to

$$n_{e,Model}(z) = \sqrt{\frac{P_e(z)}{\alpha_{eff,300}(z) \times (T_e/300)^{\beta} \times (T_j/300)^{\gamma}}} \quad (12)$$

Setting T_j = 150 K and $\gamma = -0.73$ as inferred from the $HCNH^+$ results reported by McLain and Adams (2009) bring about a reduction of the $n_{e,Model}(z)$ values determined through Eq. (5) by about 22%. Note, however, that this somewhat drastic decrease only is realized by the assumption that the vast majority of the ion population in Titan's upper atmosphere has similarly strong negative ion temperature dependencies as suggested for $HCNH^+$ by McLain and Adams (2009). If the strong negative ion temperature dependence only is applied for $HCNH^+$ the $n_{e,Model}(z)$ values is decreased by less than 5%. Vigren et al. (2012a), Smith et al. (1978) argued that rotational state effects for the nitrile ions CH_3CNH^+, $HCCCNH^+$, CH_2CHCNH^+ and $CH_3CH_2CNH^+$ probably are small as the ground states of the

ions are likely to be crossed by several repulsive potential energy surfaces. McLain and Adams (2009) showed that the dissociative recombination for a series of proton bounded nitrile dimer ions proceeds mainly through the direct mechanism with nearly no dependence on the rotational temperature of the ions. In one of the pioneering works concerning the indirect mechanism of dissociative recombination Bardsley (1968) stated that the electron capture rate to a first approximation is proportional to the square root of the ion's rotational temperature. A positive rotational temperature dependence may for example be inferred for the dissociative recombination of N_2H^+ considering the T_e and T dependencies obtained in storage ring and FALP experiments, respectively (Vigren et al., 2012b; Lawson et al., 2011). In summary it seems reasonable that while some Titan ions may have negative T_j dependencies for dissociative recombination, other have positive T_j dependencies, and most complex ions only weak T_j dependencies. Though encouraging further investigations into the influence of T_j in recombination reactions we deem it unlikely that our high estimate of the effective recombination coefficient in Titan's ionosphere (Eq. (10)) is significantly lower than the actual value. To this end we raise finally a concern about the strong negative temperature dependence ($T^{-1.38}$) reported for the dissociative recombination of $HCNH^+$ by McLain and Adams (2009). Two of the crucial chemical reactions controlling the chemistry in the experimental plasma were in the data analysis treated as temperature independent: the proton transfer reaction $H_3^+ + HCN \rightarrow HCNH^+ + H_2$ and the three body reaction $HCNH^+ + HCN + He \rightarrow (HCN)_2H^+ + He$. This disagrees with experimental results reported for the reactions (Clary et al., 1985; Chatterjee and Johnsen, 1987).

5.4.3. Negative ions

Thermal electrons may in addition to dissociative recombination also be lost by electron attachment to molecules (and negative ions) and macromolecules. If the resulting negative ions then react with positive ions yielding neutral products the net effect of the reaction sequence is the loss of an electron (and a positive ion) from the gas phase. Negative ions (detected by the CAPS/ELS) have been reported to exist only on the level of a few percentage compared with free electrons in the considered altitude range (above 1050 km) (Coates et al., 2007). The observed low abundances of negative ions near 1200 km do not necessarily exclude an active anion chemistry proceeding there. The low abundance of negative ions may result from a balance between rapid production and loss processes. In addition the charge state of the negative ions is not fully known. Coates et al. (2007) argued that the heaviest negative ions observed by the ELS instrument could have a charge state as high as −5.

Near 1200 km the loss rate of electrons due to dissociative recombination is roughly $L_e(\mathrm{DR}) = 5 \times 10^{-4}\ \mathrm{s}^{-1}$. The electron loss rate due to the reaction sequence electron attachment onto molecules (either radiative or dissociative), EA, followed by mutual neutralization (reaction between positive and negative ions forming neutral products), MN, is given by the sum

$$L_e(\mathrm{EA}+\mathrm{MN}) = \sum_j k_{EA,j} n_j f_j \quad (13)$$

where $k_{EA,j}$ is the rate coefficient for electron attachment onto species j, n_j is the number density of j and f_j is the fraction of the negative ions produced by the electron attachment onto j that will be removed by mutual neutralization with positive ions. It is noted that $k_{EA,j}$, n_j and f_j are anticipated to change with altitude due to electron temperature changes and compositional changes. While many neutral species have k_{EA} values below $10^{-16}\ \mathrm{cm}^3\ \mathrm{s}^{-1}$ and even below $10^{-20}\ \mathrm{cm}^3\ \mathrm{s}^{-1}$ there are examples of neutral molecules (e.g. C_4H and C_6H) with high electron affinities and rate coefficients approaching 10^{-8} and even $10^{-7}\ \mathrm{cm}^3\ \mathrm{s}^{-1}$ at electron temperatures of 300 K (Herbst and Osamura, 2008).

The relative importance of the various processes removing a given negative ion species from the gas-phase is difficult to assess and not within the scope of the present work. There is at present a limited knowledge on the rate coefficients for reactions between "Titan-like" positive and negative ions. Recent studies on the mutual neutralization of Kr^+ and Ar^+ with a series of molecular anions (e.g., Br_2^-, NO_3^-, SF_6^-) revealed rate coefficients spanning from about 3×10^{-8} to $6 \times 10^{-8}\ \mathrm{cm}^3\ \mathrm{s}^{-1}$ at room temperature (see Miller et al., 2012 and references therein) and with temperature dependencies of about $(T/300)^{-0.9}$ in the temperature regime from 300 to 550 K. Earlier experimental studies (e.g., Smith et al., 1978, see also Hickman, 1979 and references therein) on mutual neutralization reactions (e.g., $N_2^+ + O_2^-$, $NO^+ + O^-$, $NH_4^+ + Cl^-$, $H_3O^+(H_2O)_3 + NO_3^-$) show rate coefficients in between about 4×10^{-8} and $5 \times 10^{-7}\ \mathrm{cm}^3\ \mathrm{s}^{-1}$ at room temperature and with temperature dependencies closer to $(T/300)^{-0.5}$. It is noted that laboratory investigations into reactions between positive and negative ions, with the use of a Double ElectroStatic Ion Ring ExpEriment (DESIREE) will be commenced within a near future (e.g., Thomas et al., 2011), thereby expanding the number of investigated reactions between positive and negative ions as to more firmly establish the range over which rate coefficients vary. From the existing laboratory data, as seen in the model work by Vuitton et al. (2009), it seems as if mutual neutralization of simple negative ions such as CN^- and C_3N^- in Titan's main ionospheric region are lost primarily through associative electron detachment with radicals such as H and CH_3 (e.g., $H + CN^- \rightarrow HCN + e^-$).

Let us hypothesize, on completely speculative bases, that there is a class of molecules, MEA, with high electron affinities, having high electron attachment rate coefficients between 10^{-8} and $10^{-7}\ \mathrm{cm}^3\ \mathrm{s}^{-1}$ and f values between 0.1 and 1. Then their total number density needs to be somewhere between 5×10^3 and $5 \times 10^5\ \mathrm{cm}^{-3}$ as for $L_e(\mathrm{EA}+\mathrm{MN})$ to be compatible with $L_e(\mathrm{DR})$. However, if f is close to 1 and the rate coefficient for electron attachment is close to $10^{-7}\ \mathrm{cm}^3\ \mathrm{s}^{-1}$ (the combination giving the lower required density of MEA) then the rate coefficient for the mutual neutralization process would need to be as high as $5 \times 10^{-6}\ \mathrm{cm}^3\ \mathrm{s}^{-1}$ to keep the steady state value of the negative ion number density below 10% of the overall negatively charged population, which we consider as an observational constraint. In fact the same requirement for the mutual neutralization rate coefficient applies for any given combination of k_{EA}, n_{MEA} and f fulfilling $k_{EA} n_{MEA} f = 5 \times 10^{-4}\ \mathrm{s}^{-1}$.

Another possible mechanism for the loss of electrons is the interaction with aerosols. The large mass negative ions observed by CAPS/ELS are considered to be aerosols at the first stages of their evolution (Coates et al., 2007; Waite et al., 2007). Electrons can readily attach at the surface of aerosols (Borucki and Whitten, 2008), thereby reducing the abundance of free electrons. Although, the efficiency of this mechanism remains to be investigated in detail, CAPS/ELS observations appear to deem it unable to explain the problem identified here. The observed CAPS spectra reveal a rapid decrease in the size of the large mass negative ions with increasing altitude (between 1000 and 1200 km) in Titan's atmosphere (Coates et al., 2009). Since the heterogeneous loss of electrons decreases rapidly with decreasing aerosol size (Borucki and Whitten, 2008), this mechanism appears unable to provide the more or less constant with altitude "factor of 2 difference" between observed and modeled electron densities.

5.5. Remarks on the relation between observed electron number densities and temperatures and calculated electron production rates

We define $\alpha^*_{eff,300}$ as the effective recombination at $T_e = 300$ K needed to bring consistency between LP observed n_e and T_e values and calculated P_e values, i.e.

$$\alpha^*_{eff,300} = \frac{P_e}{n^2_{e,LP}}(T_{e,LP}/300)^{0.7} \quad (14)$$

In Fig. 12 $\alpha^*_{eff,300}(P_e, n_{e,LP}, T_{e,LP})$ is plotted against the ambient N_2 density along the Cassini trajectories, using data (below 1200 km) from the T40, T41, T42 and T48 Titan flybys. The best fit of the data to a logarithmic function (shown as a solid black line in Fig. 12) is given by

$$\alpha^*_{eff,300}(n(N_2)) = (6.057 \times 10^{-2} \times \ln(n(N_2)) - 0.983) \times 10^{-5} \quad (15)$$

with $\alpha^*_{eff,300}$ in $cm^3\ s^{-1}$ and $n(N_2)$ in cm^{-3}. The dashed lines shown in Fig. 12 are located at positions of $(1 \pm D) \times$ "Best fit value", where D relates to the goodness-of-fit (relative error) to the observed data. The D value (=0.104) for the fit of $\alpha^*_{eff,300}$ versus $n(N_2)$ is given by

$$D = \sqrt{\frac{1}{N}\sum_{i=1}^{N}\left(1 - \frac{\alpha^*_{eff,300,observed}(n(i))}{\alpha^*_{eff,300,fit}(n(i))}\right)} \quad (16)$$

with n here being the N_2 density and N (=48) being the total number of data points.

It is seen in Fig. 12 that the vast majority of the points are within 10% of the best-fit prediction. This is remarkable considering the statistical uncertainties associated with the parameters of Eq. (14). There is a larger relative spread of the values at low N_2 densities. This may for example be due to transport effects, which may come into play at higher altitudes, and due to higher statistical uncertainties for the measurements of lower electron densities.

In Table 7 we present the best fits (and associated D values) of $\alpha^*_{eff,}(P_e, n_{e,LP})$ and $\alpha^*_{eff,300}(P_e, n_{e,LP}, T_{e,LP})$ as a function of altitude, ambient N_2 and CH_4 number densities and the N_2 column density in the line of sight towards the Sun. Note that $\alpha^*_{eff,}$ values are obtained as follows:

$$\alpha^*_{eff} = \frac{P_e}{n^2_{e,LP}} \quad (17)$$

As an interesting example $\alpha^*_{eff,300,fit}(z)$ is $3 \times 10^{-6}\ cm^3\ s^{-1}$ at 1150 km while within 10% of $4 \times 10^{-6}\ cm^3\ s^{-1}$ in between 1000 and 1100 km. While awaiting explanations for the discrepancy found between modeled and observed electron densities, the functions in Table 7 may be used together with P_e predictions (based on an thermospheric model) to estimate electron densities in Titan's sunlit main ionospheric region. It is stressed, however, that the given α^*_{eff} and $\alpha^*_{eff,300}$ values are unlikely to resemble the actual effective electron dissociative recombination coefficients in Titan's upper atmosphere (see Section 4).

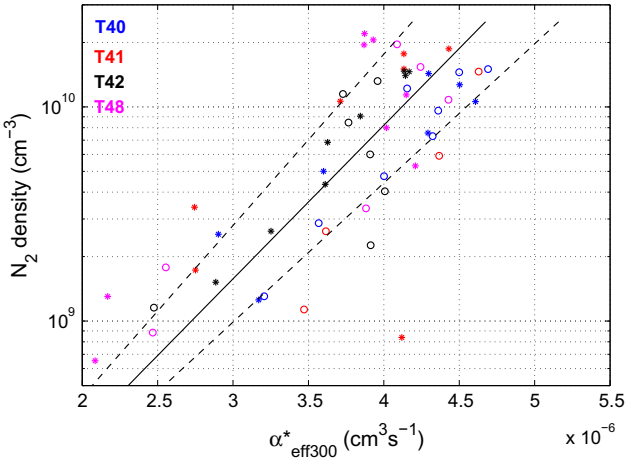

Fig. 12. Values of $\alpha^*_{eff,300}(P_e, n_{e,LP}, T_e)$ (see Eq. (15)) plotted against the ambient N_2 density along the Cassini trajectories for the T40 (blue), T41 (red), T42 (black) and T48 (magenta) Titan flybys. Inbound and outbound points are marked with asterisks (*) and open circles (o), respectively. The solid black line is the best fit to a logarithmic function of the data (Eq. (15)) and the dashed lines are located at positions of $(1 \pm D) \times$ "Best fit value" where $D = 0.104$ has been derived based on Eq. (16). (For interpretation of the references to color in this figure legend, the reader is referred to the web version of this article.)

6. Conclusions

We have studied the thermal electron balance in Titan's sunlit upper atmosphere following a recent re-calibration of the INMS instrument, implying that earlier derived neutral densities should be increased by a factor of about 2.9. Our key assumptions in predicting electron number densities in the altitude range between 1050 and 1200 km (where we have made estimates of the effective recombination coefficients as presented in Section 4) have been that photochemical equilibrium applies and that free electrons are lost exclusively through dissociative recombination.

The new density profiles of N_2 and CH_4 bring a reasonable agreement between the altitudes where the electron production rates are calculated to peak and the altitudes where the electron number densities are observed to peak (see Sections 5.1 and 5.3). As shown in Figs. 1 and 11 the photochemical equilibrium model captures the measured electron number densities fairly well in a relative sense.

In Figs. 1 and 11 (as well as in Table 4), however, it is also seen that the n_e values predicted via Eq. (5) are up to a factor of about 2 higher than the LP-derived n_e values (even when using what we consider being a high estimate of $\alpha_{eff,300}$). Such pronounced discrepancies are not seen in similar studies of the thermal electron balance in the ionospheres of Venus and Mars (see e.g., Cravens et al., 1981; Mendillo et al., 2011), and we have argued that systematic errors of the input parameters of Eq. (5) and of the electron density measurements are highly unlikely to be the sole cause of the large discrepancy found. It is likely that we are missing a vital loss mechanism of electrons in our calculations, which only takes into account dissociative recombination. Reactions associated with negative ions may be important for the thermal electron balance in Titan's upper atmosphere. For the reaction sequence "electron attachment followed by mutual neutralization" to be compatible with dissociative recombination as a loss process of free electrons, it seems that a few requirements need to be fulfilled. Not only must there be a set of molecules with rate coefficient for electron attachment in the vicinity of $10^{-7}\ cm^3\ s^{-1}$, the total density of these molecules must (at least) be an order of magnitude higher than the electron number density. In addition, from observational constraints, the negative ions formed in the electron attachment processes need to react with positive ions with an average rate coefficient exceeding $5 \times 10^{-6}\ cm^3\ s^{-1}$ (otherwise it becomes difficult to explain the low abundances of negative ions observed near 1200 km). It seems improbable that there exists a set of molecules fulfilling all of these requirements. Further experimental and theoretical works establishing rate coefficients for processes associated with the production and loss of molecular anions would be very valuable. Aerosols could have an influence as an additional loss process of electrons in regions of Titan's ionosphere. In Section 5.4.3 we emphasized, however, that the heterogeneous loss process appears unable to explain the nearly constant with altitude "factor of 2 difference" between observed and modeled electron densities. In Fig. 1 it is seen that electron densities are also over-predicted at altitudes between 1200 and 1400 km. This may, at least in part, be due to the increased importance of (upwards) vertical transport present on the dayside and not accounted for in the calculations (see Cravens et al., 2010; Cui et al., 2010).

In conclusion further investigations are required to firmly establish why the discrepancy between predicted and observed

Table 7
Fit results of α^*_{eff} (Eq. (17)) and $\alpha^*_{eff,300}$ (Eq. (14)) versus altitude, ambient CH_4 density, ambient N_2 density and N_2 column density in the line of sight towards the Sun. Included in the first column are the regimes over which the equations are applicable. The *D*-values within brackets are a goodness-of-fit-parameter explained in the text and as an example through Eq. (16).

	α^*_{eff} (10^{-5} cm^3 s^{-1})	$\alpha^*_{eff,300}$ (10^{-5} cm^3 s^{-1})
z (km) $1000 < z < 1200$	$6.107 \times 10^{-7} \times z^2 - 2.267 \times 10^{-3} \times z + 1.973$ [$D = 0.171$]	$-3.466 \times 10^{-6} \times z^2 + 6.628 \times 10^{-3} \times z - 2.734$ [$D = 0.122$]
$n(CH_4)$ (cm^{-3}) $3 \times 10^7 < n < 3 \times 10^8$	$8.059 \times 10^{-2} \times \ln(n) - 1.254$ [$D = 0.172$]	$7.389 \times 10^{-2} \times \ln(n) - 0.998$ [$D = 0.134$]
$n(N_2)$ (cm^{-3}) $5 \times 10^8 < n < 2 \times 10^{10}$	$5.946 \times 10^{-2} \times \ln(n) - 1.089$ [$D = 0.145$]	$6.057 \times 10^{-2} \times \ln(n) - 0.983$ [$D = 0.104$]
$C(N_2)$ (cm^{-2}) $10^{15} < C < 1.6 \times 10^{17}$	$5.825 \times 10^{-2} \times \ln(C) - 1.984$ [$D = 0.166$]	$5.937 \times 10^{-2} \times \ln(C) - 1.896$ [$D = 0.115$]

electron number densities in Titan's sunlit upper atmosphere exists below 1200 km. A combination of missing loss processes and systematic errors of input parameters cannot be ruled out. Following our sensitivity studies and discussions in Section 5.4 a few of the open questions remaining include:

- What is the influence of the rotational temperature of the ions in the dissociative recombination of the major ions in Titan's upper atmosphere? In particular, what is the effect on the rate coefficients at $T_e = 300$ K, when the rotational temperature of the ions is decreased from $T_{rot} = 300$ K to $T_{rot} = 150$ K?
- What causes the discrepancy between the calculated electron temperatures (Richard et al., 2011) and the LP-derived values in the deep ionosphere?
- What is the charge state of negative ions in Titan's upper atmosphere? Is it possible that there is a non-negligible difference in the number densities of positive ions compared with free electrons even at $z > 1050$ km?
- What is the range of rate coefficients for reactions between positive and negative molecular ions at the temperatures prevailing in Titan's ionosphere?
- Could a class of molecules with high rate coefficients for electron attachment exist in high enough abundance in Titan's upper atmosphere such that the loss rate of electrons, due to the reaction sequence electron attachment followed by mutual neutralization, becomes comparable with the loss rate due to dissociative recombination?
- How is the thermal electron balance in Titan's upper atmosphere affected by the interaction of aerosols with the ionosphere?

Acknowledgments

E.V. is grateful for funding from the Swedish Research Council (Contract No. 2011-894). M.G. is partially funded by the Science & Technology Facilities Council (STFC) through the rolling grant to Imperial College, London. We acknowledge support from the EU through the FP7/DEPTH grant. D.F.S. was supported by the Cassini–Huygens Mission through JPL Contract No. 109303. R.V.Y. acknowledges support of NASA Grant NNX09AB58G. This work was performed in the framework of the Marie Curie International Research Staff Exchange Scheme PIRSES-GA-2009-247509. We thank the TIMED/SEE PI, Tom Woods, and his team for providing us with the solar flux dataset and associated routines of extrapolation to planets.

Appendix A. Electron energy degradation model

The first step in the calculation of the secondary electron production rate, $P_{e,sec}(z)$, involves the distribution of photoelectrons onto an energy grid $k = 1,2,\ldots$ with a bin width of 1 eV. The highest energy bin considered is $k = N_E = 12{,}400$. Note that 12,400 eV roughly corresponds to the energy of a photon having a wavelength of 0.1 nm. As an example photons in the wavelength interval 26.0–27.0 nm (47.686–45.920 eV) may for instance produce N_2^+ in the $B^2\sum_u^+$ state, the threshold energy of which is 18.751 eV. The photoelectrons, thereby produced, have energies between 27.169 and 28.935 eV and in the code we let in this particular case the photoelectrons be uniformly distributed in $k = 28$ and $k = 29$. The photoelectron spectrum is generated considering all combinations of wavelength intervals and single ionization processes (the contribution from double and triple ionization processes is minute and neglected throughout the calculations).

The secondary electron production rate is determined through a recursive approach. First we consider the X electrons in the highest energy bin. Based on the ambient N_2 and CH_4 number densities and energy-dependent absolute cross sections for electron impact ionization and electron excitation processes we calculate the expected fraction, $f(k = N_E)$, of electrons in the energy bin $k = N_E$ that will lose energy by causing ionizations. The complementary fraction $1 - f(k = N_E)$ of the electrons in the energy bin $k = N_E$ lose energy by causing electronic excitations (not involving ionization). In addition to densities and energy-dependent cross-sections, we use the threshold energies of the various electron-impact processes to calculate expectation values of the *total* kinetic energy loss, $I(k = N_E)$ and $E(k = N_E)$, associated with the electron impact induced ionization and electronic excitation processes, respectively.

The ionization events yield the production of $f(k = N_E)X$ new electrons. These electrons are distributed to lower energy bins using a discrete approximation of the formula presented in Rees (1989) for the energy distribution of secondary electrons ejected in electron impact ionization events of N_2 (which is a function of the incident electron energy). If a fraction of the secondary electrons is added to the bin k', then a similar fraction of the primary electrons is added to the bin k^* fulfilling energy conservation, i.e., $k' + k^* = N_E - I(k = N_E)$. The $(1 - f(k = N_E))X$ that cause electronic excitation are simply added to the energy bin $k = N_E - E(k = N_E)$.

We then move to the next energy bin $k = N_E - 1$ and perform similar calculations as described above for $k = N_E$. We then continue towards lower and lower energy bins until we have completed calculations for the electrons in the 14 eV energy bin, just above the lowest ionization potential of CH_4. The secondary electron production rate is finally obtained by summing the newly created electrons introduced in each step of the calculation.

References

Ågren, K. et al., 2009. On the ionospheric structure of Titan. Planet. Space Sci. 57, 1821–1827.
Ågren, K., Edberg, N.J.T., Wahlund, J.-E., 2012. Detection of negative ions in the deep ionosphere of Titan during the Cassini T70 flyby. Geophys. Res. Lett. 39, L10201.
Amitay, Z. et al., 1996. Dissociative recombination of CH^+: Cross section and final states. Phys. Rev. A 54, 4032–4050.
Bardsley, J., 1968. The theory of dissociative recombination. J. Phys. B 1, 365–368.
Borucki, W.J., Whitten, R.C., 2008. Influence of high abundances of aerosols on the electrical conductivity of the Titan atmosphere. Planet. Space Sci. 56, 19–26.
Chatterjee, B.K., Johnsen, R., 1987. Clustering reactions of H_2CN^+ ions with HCN. J. Chem. Phys. 87, 2399–2400.

Clary, D.C., Smith, D., Adams, N.G., 1985. Temperature dependence of rate coefficients for reactions of ions with dipolar molecules. Chem. Phys. Lett. 119, 320–326.

Coates, A.J., Crary, F.J., Lewis, G.R., Young, D.T., Waite Jr., J.H., Sittler Jr., E.C., 2007. Discovery of heavy negative ions in Titan's ionosphere. Geophys. Res. Lett. 34, L22103. http://dx.doi.org/10.1029/2007GL030978.

Coates, A.J. et al., 2009. Heavy negative ions in Titan's ionosphere: Altitude and latitude dependence. Planet Space Sci. 57, 1866–1871.

Crary, F.J., Magee, B.A., Mandt, K., Waite Jr., J.H., Westlake, J., Young, D.T., 2009. Heavy ions, temperatures and winds in Titan's ionosphere: Combined Cassini CAPS and INMS observations. Planet. Space Sci. 57, 1847–1856.

Cravens, T.E., Kliore, T.E., Kozyra, J.U., Nagy, A.F., 1981. The ionospheric peak on the Venus dayside. J. Geophys. Res. 86 (A13), 323–329.

Cravens, T.E. et al., 2005. Titan's ionosphere: Model comparisons with Cassini Ta data. Geophys. Res. Lett. 32, L12108.

Cravens, T.E. et al., 2006. Composition of Titan's ionosphere. Geophys. Res. Lett. 33, L07105. http://dx.doi.org/10.1029/2005GL025575.

Cravens, T.E. et al., 2009. Model-data comparisons for Titan's nightside ionosphere. Icarus 199, 174–188.

Cravens, T.E. et al., 2010. Dynamical and magnetic field time constants for Titan's ionosphere: Empirical estimates and comparisons with Venus. J. Geophys. Res. 115, A08319.

Cui, J. et al., 2009. Diurnal variations of Titan's ionosphere. J. Geophys. Res. 114, A06310.

Cui, J. et al., 2010. Ion transport in Titan's upper atmosphere. J. Geophys. Res. 115, A06314.

Cui, J. et al., 2012. The CH_4 structure in Titan's upper atmosphere revisited. J. Geophys. Res. 117, E11006. http://dx.doi.org/10.1029/2012JE004222.

Danielsson, M. et al., 2008. The cross-section and branching fractions for dissociative recombination of the diacetylene cation $C_4D_2^+$. Int. J. Mass Spectrom. 273, 111–116.

Ehlerding, A. et al., 2003. Rates and products of the dissociative recombination of $C_3H_7^+$ in low-energy electron collisions. J. Phys. Chem. A 107, 2179–2184.

Ehlerding, A. et al., 2004. Dissociative recombination of C_2H^+ and $C_2H_4^+$: Absolute cross sections and product branching ratios. Phys. Chem. Chem. Phys. 6, 949–954.

Erwin, D.A., Kunc, J.A., 2005. Electron-impact dissociation of the methane molecule into neutral fragments. Phys. Rev. A 72, 052719–052724.

Erwin, D.A., Kunc, J.A., 2008. Dissociation and ionization of the methane molecule by nonrelativistic electrons including the near threshold region. J. Appl. Phys. 103, 064906–064914.

Fox, J.L., 2007. Near-terminator Venus ionosphere: How Chapman-esque? J. Geophys. Res. 112, E04S02.

Fox, J.L., Yeager, K.E., 2006. Morphology of the near-terminator martian ionosphere: A comparison of models and data. J. Geophys. Res. 111, A10309.

Galand, M., Yelle, R.V., Coates, A.J., Backes, H., Wahlund, J.-E., 2006. Electron temperature of Titan's sunlit ionosphere. Geophys. Res. Lett. 33, L21101.

Galand, M., Moore, L., Charnay, B., Mueller-Wodarg, I., Mendillo, M., 2009. Solar primary and secondary ionization at Saturn. J. Geophys. Res. 114, A06313.

Galand, M. et al., 2010. Ionization sources in Titan's deep ionosphere. J. Geophys. Res. 115, A07312.

Galand, M., Coates, A.J., Cravens, T.E., Wahlund, J.-E., 2013. Titan's ionosphere. In: Mueller-Wodarg, I., Griffith, C., Lellouch, E., Cravens, T.E. (Eds.), Titan: Surface, Atmosphere, and Magnetosphere. Cambridge University Press (Cambridge Planetary Science Series), in press.

Geppert, W.D. et al., 2004. Dissociative recombination of nitrile ions: $DCCCN^+$ and $DCCCND^+$. Astrophys. J. 613, 1302–1309.

Hamberg, M. et al., 2011. Experimental studies of the dissociative recombination processes for the $C_6D_6^+$ and $C_6D_7^+$ ions. In: Joblin, C., Tielens, A.G.G.M. (Eds.), PAHs and the Universe. EAS Publication Series, pp. 241–249.

Herbst, E., Osamura, Y., 2008. Calculations of the formation rates and mechanisms for C_nH anions in interstellar and circumstellar media. Astrophys. J. 679, 1670–1679.

Hickman, A.P., 1979. Approximate scaling formula for ion–ion mutual neutralization rates. J. Chem. Phys. 70, 4872–4878.

Itikawa, Y., 2006. Cross sections for electron collisions with nitrogen molecules. J. Phys. Chem. Ref. Data 35, 31–53. http://dx.doi.org/10.1063/1.1937426.

Kaminska, M. et al., 2010. Dissociative recombination of CH_5^+ and CD_5^+; Measurement of the product branching fractions and the absolute cross sections, and the breakup dynamics in the $CH_3 + H + H$ product channel. Phys. Rev. A 81, 062701, 11pp.

Kliore, A.J., Nagy, A.F., Cravens, T.E., Richard, M.S., Rymer, A.M., 2011. Unusual electron density profiles observed by Cassini radio occultations in Titan's ionosphere: Effects of enhanced magnetospheric electron precipitation? J. Geophys. Res. 116, A11318.

Koskinen, T.T., Yelle, R.V., Snowden, D.S., Lavvas, P., Sandel, B.R., Capalbo, F.J., Benilan, Y., West, R.A., 2011. The mesosphere and thermosphere of Titan revealed by Cassini/UVIS stellar occultations. Icarus 216, 507–534.

Laframboise, J.G., Godard, R., 1974. Perturbation of an electrostatic probe by a spacecraft at small speed ratios. Planet. Space Sci. 22, 1145–1155.

Larsson, M., Orel, A.E., 2008. Dissociative Recombination of Molecular Ions. Cambridge Univ. Press, New York.

Lavvas, P., Galand, M., Yelle, R.V., Heays, A.N., Lewis, B.R., Lewis, G.R., Coates, A.J., 2011. Energy deposition and primary chemical products in Titan's upper atmosphere. Icarus 213, 233–251.

Lawson, P.A., Osborne Jr., D., Adams, N.G., 2011. Effect of isotopic content on the rate constants for the dissociative electron–ion recombination of N_2H^+. Int. J. Mass Spectrom. 304, 41–44.

Lean, J.L. et al., 2011. Solar extreme ultraviolet irradiation: Present, past and future. J. Geophys. Res. 116, A01102.

Liu, X., Shemansky, D.E., 2006. Analysis of electron impact ionization properties of methane. J. Geophys. Res. 111, A04303.

Luhmann, J.G. et al., 2012. Investigating magnetospheric interaction effects on Titan's ionosphere with the Cassini orbiter Ion Neutral Mass Spectrometer, Langmuir probe and magnetometer observations during targeted flybys. Icarus 219, 534–555.

Ma, Y. et al., 2006. Comparisons between MHD model calculations and observations of Cassini flybys of Titan. J. Geophys. Res. 111, A05207.

Majeed, T., Strickland, D.J., 1997. New survey of electron impact cross sections for photoelectron and auroral electron energy loss calculations. J. Phys. Chem. Ref. Data 26, 335–349.

Martinis, C.R., Wilson, J.K., Mendillo, M.J., 2003. Modeling day-to-day ionospheric variability on Mars. J. Geophys. Res. 108, A10, 1383, 6pp.

McLain, J.L., Adams, N.G., 2009. Flowing afterglow studies of temperature dependencies for electron dissociative recombination of $HCNH^+$, CH_3CNH^+ and $CH_3CH_2CNH^+$ and their symmetrical proton-bound dimers. Planet. Space Sci. 57, 1642–1647.

McLain, J.L., Poterya, V., Molek, C.D., Babcock, L.M., Adams, N.G., 2004. Flowing afterglow studies of the temperature dependencies for dissociative recombination of O_2^+, CH_5^+, $C_2H_5^+$, and $C_6H_7^+$ with electrons. J. Phys. Chem. A 108, 6706–6708.

McLain, J.L., Poterya, V., Molek, C.D., Jackson, D.M., Babcock, L.M., Adams, N.G., 2005. $C_3H_3^+$ isomers: Temperature dependencies of production in the H_3^+ reaction with allene and loss by dissociative recombination with electrons. J. Phys. Chem. A 109, 5119–5123.

Mendillo, M., Lollo, A., Withers, P., Matta, M., Pätzold, M., Tellmann, S., 2011. Modeling Mars' ionosphere with constraints from same-day observations by Mars Global Surveyor and Mars Express. J. Geophys. Res. 116, A11303.

Miller, T.M., Shuman, N.S., Viggiano, A.A., 2012. Behavior of rate coefficients for ion–ion mutual neutralization, 300–550 K. J. Chem. Phys. 136, 204306, 7pp.

Moore, L., Mueller-Wodarg, I., Galand, M., Kliore, A., Mendillo, M., 2010. Latitudinal variations in Saturn's ionosphere: Cassini measurements and model comparisons. J. Geophys. Res. 115, A11317.

Moses, J.I., Bass, S.F., 2000. The effects of external material on the chemistry and structure of Saturn's ionosphere. J. Geophys. Res. 105, 7013–7052.

Novotny, O. et al., 2005. Recombination of polycyclic aromatic hydrocarbon photoions with electrons in a flowing afterglow plasma. J. Chem. Phys. 123, 104303, 6pp.

Öjekull, J. et al., 2004. Dissociative recombination of NH_4^+ and ND_4^+ ions: Storage ring experiments and ab initio molecular dynamics. J. Chem. Phys. 120, 7391–7399.

Öjekull, J. et al., 2006. Dissociative recombination of ammonia clusters studied by storage ring experiments. J. Chem. Phys. 125, 194306, 9pp.

Osborne Jr., D., Lawson, P.A., Adams, N.G., 2011. Flowing afterglow studies of dissociative electron–ion recombination for a series of single ring compounds at room temperature. Int. J. Mass Spectrom. 305, 35–39.

Osepian, A., Kirkwood, S., Dalin, P., Tereschenko, V., 2009. D-region electron density and effective recombination coefficients during twilight – Experimental data and modeling during solar proton events. Ann. Geophys. 27, 3713–3724.

Peterson, J.R. et al., 1998. Dissociative recombination and excitation of N_2^+: Cross sections and product branching ratios. J. Chem. Phys. 108, 1978–1988.

Rasmussen, C.E., Schunk, R.W., Wickwar, V.B., 1988. A photochemical equilibrium model for ionospheric conductivity. J. Geophys. Res. 93, 9831–9840.

Rees, M.H., 1989. Physics and Chemistry of the Upper Atmosphere. Cambridge Univ. Press, New York.

Richard, M.S. et al., 2011. Energetics of Titan's ionosphere: Model comparisons with Cassini data. J. Geophys. Res. 116, A09310. http://dx.doi.org/10.1029/2011JA016603.

Robertson, I.P. et al., 2009. Structure of Titan's ionosphere: Model comparisons with Cassini data. Planet. Space Sci. 57, 1834–1846. http://dx.doi.org/10.1016/j.pss.2009.07.011.

Roboz, A., Nagy, A., 1994. The energetics of Titan's ionosphere. J. Geophys. Res. 99 (A2), 2087–2093.

Samson, J.A.R., Masuoka, T., Pareek, P.N., Angel, G.C., 1987. Total and dissociative photoionization cross sections of N_2 from threshold to 107 eV. J. Chem. Phys. 86, 6128–6132.

Samson, J.A.R., Haddad, G.N., Masuoka, T., Pareek, P.N., Kilcoyne, D.A.L., 1989. Ionization yields, total absorption, and dissociative photoionization cross sections of CH_4 from 110–950 Å. J. Chem. Phys. 90, 6925–6932.

Semaniak, J. et al., 2001. Dissociative recombination of $HCNH^+$: Absolute cross-sections and branching ratios. Astrophys. J. Suppl. Ser. 135, 275–283.

Sheehan, C.H., St-Maurice, J.-P., 2004. Dissociative recombination of the methane family ions: rate coefficients and implications. Adv. Space Res. 33, 216–220.

Shemansky, D.E., Liu, X., 2005. Evaluation of electron impact excitation of $N_2X^1\Sigma_g^+(0)$ into the $N_2^+X^2\Sigma_g^+(v)$, $A^2\Pi_u^+(v)$ and $B^2\sum_u^+(v)$ states. J. Geophys. Res. 110, A07307. http://dx.doi.org/10.1029/2005JA011062.

Smith, D., Church, M.J., Miller, T.M., 1978. Mutual neutralization of simple and clustered positive and negative ions. J. Chem. Phys. 68, 1224–1229.

Stolte, W.C., He, Z.X., Cutler, J.N., Lu, Y., Samson, J.A.R., 1998. Dissociative photoionization cross sections of N_2 and O_2 from 100 to 800 eV. Atom Data Nucl. Data Tables 69, 171–179.

Strobel, D.F., 2010. Molecular hydrogen in Titan's atmosphere: Implications of the measured tropospheric and thermospheric mole fractions. Icarus 208, 878–886.
Sundström, G. et al., 1994. Destruction rate of H_3^+ by low-energy electrons measured in a storage-ring experiment. Science 263, 785–787.
Thomas, R.D., 2008. When electrons meet molecular ions and what happens next: Dissociative recombination from interstellar molecular clouds to internal combustion engines. Mass Spectrom. Rev. 27, 485–530.
Thomas, R.D. et al., 2011. DESIREE: A unique cryogenic electrostatic storage ring for merged ion-beams studies. J. Phys. Conf. Ser. 300, 012011, 8pp.
Thomas, R.D. et al., 2012. Dissociative recombination of vibrationally cold CH_3^+ and interstellar implications. Astrophys. J. 758, 55, 9pp.
Titheridge, J.E., 1997. Model results for the ionospheric E region: Solar and seasonal changes. Ann. Geophys. 15, 63–78.
Vigren, E. et al., 2008. Dissociative recombination of fully deuterated protonated acetonitrile, CD_3CND^+: Product branching fractions, absolute cross section and thermal rate coefficient. Phys. Chem. Chem. Phys. 10, 4014–4019.
Vigren, E. et al., 2009. The dissociative recombination of protonated acrylonitrile, CH_2CHCNH^+, with implications for the nitrile chemistry in dark molecular clouds and the upper atmosphere of Titan. Astrophys. J. 695, 317–324.
Vigren, E. et al., 2010. Dissociative recombination of the acetaldehyde cation, CH_3CHO^+. Phys. Chem. Chem. Phys. 12, 11670–11673.
Vigren, E. et al., 2012a. Dissociative recombination of nitrile ions with implications for Titan's upper atmosphere. Planet. Space Sci. 60, 102–106.
Vigren, E. et al., 2012b. Reassessment of the dissociative recombination of N_2H^+ at CRYRING. Astrophys. J. 757, 34, 4pp.
Vuitton, V., Yelle, R.V., Anicich, V.G., 2006. The nitrogen chemistry of Titan's upper atmosphere revealed. Astrophys. J. 647, 175–178.
Vuitton, V., Yelle, R.V., McEwan, M.J., 2007. Ion chemistry and N-containing molecules in Titan's upper atmosphere. Icarus 191, 722–742.
Vuitton, V., Yelle, R., Cui, J., 2008. Formation and distribution of benzene on Titan. J. Geophys. Res. 113, E05007.
Vuitton, V. et al., 2009. Negative ion chemistry in Titan's upper atmosphere. Planet. Space. Sci. 57, 1558–1572.
Wahlund, J.-E. et al., 2005. Cassini measurements of cold plasma in the ionosphere of Titan. Science 308, 986–989.
Wahlund, J.-E. et al., 2009. On the amount of heavy molecular ions in Titan's ionosphere. Planet. Space Sci. 57, 1857–1865.
Waite Jr., J.H. et al., 1997. Outer planet ionospheres: A review of recent research and a look toward the future. Adv. Space Res. 20, 243–252.
Waite, J.H. et al., 2004. The Cassini ion and Neutral Mass Spectrometer (INMS) investigation. Space Sci. Rev. 114, 113–231.
Waite Jr., J.H. et al., 2007. The process of tholin formation in Titan's upper atmosphere. Science 316, 870–875.
Westlake, J.H. et al., 2012. Titan's ionospheric composition and structure: Photochemical modeling of Cassini INMS data. J. Geophys. Res. 117, E01003.
Woods, T.N., 2008. Recent advances in observations and modeling of the solar ultraviolet and X-ray spectral irradiance. Adv. Space Res. 42, 895–902.
Woods, T.N. et al., 2005. Solar EUV Experiment: Mission overview and first results. J. Geophys. Res. 110, A01312.
Woods, T.N. et al., 2008. XUV photometer system (XPS): Improved solar irradiance algorithm using CHIANTI spectral models. Solar Phys. 250, 235–267.
Yelle, R.V., Miller, S., 2004. Jupiter's thermosphere and ionosphere. In: Bagenal, F. et al. (Eds.), Jupiter: The planet, Satellites, and Magnetosphere. Cambridge University Press, New York, pp. 185–218.
Zhaunerchyk, V. et al., 2007. Dissociative recombination study of N_3^+: Cross section and branching fraction measurements. J. Chem. Phys. 127, 014305, 5pp.
Zhaunerchyk, V. et al., 2008. Dissociative recombination dynamics of the ozone cation. Phys. Rev. A 77, 022704, 9pp.